Journal of the American Ceramic Society

RESEARCH ARTICLE OPEN ACCESS

Toughening of TiO_2 via Femtosecond Laser Shock Peening

Anish Bajla[1] | Shubha Majumder[1] | Subah Mubassira[2] | Ke Xu[3] | Xuanyu Sheng[3] | Joshua A. Medina[4] | Het Jani[1] | Colin McMillen[5] | Luiz G. Jacobsohn[4] | Haiyan Wang[3] | Xinghang Zhang[3] | Shuozhi Xu[2] | Xin Zhao[1] | Yifan Zhang[1]

[1]Department of Mechanical Engineering, Clemson University, Clemson, South Carolina, USA | [2]School of Aerospace and Mechanical Engineering, University of Oklahoma, Norman, Oklahoma, USA | [3]School of Materials Engineering, Purdue University, West Lafayette, Indiana, USA | [4]Department of Materials Science and Engineering, Clemson University, Clemson, South Carolina, USA | [5]Department of Chemistry, Clemson University, Clemson, South Carolina, USA

Correspondence: Yifan Zhang (yifan3@clemson.edu)

Received: 25 February 2026 | **Revised:** 6 July 2026 | **Accepted:** 9 July 2026

Keywords: defects | femtosecond laser shock peening | indentation fracture resistance | stacking faults | TiO_2

ABSTRACT

Most ceramics have low fracture toughness (<5 MPa $\sqrt{m}$) at room temperature. This work explores the feasibility of toughening TiO_2 via femtosecond laser shock peening (fs-LSP). Transmission electron microscopy (TEM) analyses reveal LSP-induced the creation of high-density stacking faults, dislocation structures, and twin boundaries in the LSP-treated surface layer (~55 μm thick) of single-crystal rutile TiO_2. Meanwhile, oxygen vacancies were introduced into TiO_2 via the LSP treatment, as evidenced by X-ray photoelectron spectroscopy (XPS) results and the red peak shifts in Raman spectra. In addition, X-ray diffraction scans show in-plane compressive residual stress (−61 to −306 MPa) built in LSP-processed TiO_2. The indentation fracture resistance (K_{IFR}) of TiO_2 is enhanced from 2.8 MPa$\sqrt{m}$ to 6.8–8.2 MPa$\sqrt{m}$. The role of compressive residual stress, oxygen vacancy, dislocations, stacking faults, and twins are discussed using atomistic simulations, semiquantitative and qualitative analyses. This study demonstrates the remarkable synergistic effects of defect networks and residual compressive stress in toughening TiO_2 and possibly other ceramic materials. Our work also qualifies the fs-LSP as an effective and scalable method to toughen ceramic materials.

1 | Introduction

Ceramic materials have a broad range of applications across various industrial sectors due to their functional versatility [1–8], exceptional mechanical strength [3, 9, 10], outstanding wear resistance [11, 12], and extraordinary thermal stability [12, 13]. Nonetheless, most ceramic materials are brittle at room temperature [14–16] with fracture toughness below 5 MPa$\sqrt{m}$, which is notably inferior to common structural metallic materials (> 20 MPa$\sqrt{m}$) [17]. Due to compact charged cores [18] and high Peierls stress incurred by their strong and directional ionic/covalent bonds [16], most ceramics have high dislocation nucleation energy barriers (1–10 eV) [19], low dislocation mobility, and limited slip systems. Therefore, crack formation prevails over dislocation-mediated plasticity in many ceramic materials deformed at room temperature.

Enhancing the toughness of ceramic materials is a long-lasting and challenging goal for the material research community. Prior studies have been inspired by nature in developing damage-tolerant ceramic materials that employ both extrinsic and intrinsic toughening mechanisms. The hierarchical "brick-and-mortar" composite structures [20, 21] and the high-density of growth nanotwins confer impressive fracture toughness in seashells [22–24] composed of $CaCO_3$ and Al_2O_3. Viable and established toughening methods for ceramics include bridging, deflecting, and branching cracks at layer interfaces, as well as at second-phase particles and grain boundaries [17]. Phase

transformation toughening in Yttria-stabilized ZrO_2 (YSZ) is another successful effort in toughening ceramics [25, 26].

Nevertheless, achieving intrinsic toughening in ceramics via microstructural defects remains challenging. Some recent studies have sought to enhance dislocation nucleation and density in ceramics via high-temperature preloading [10], mechanical seeding [27–29], nonequilibrium processing [13, 30–32], the construction of coherent ceramic-based hetero-phase interfaces [33, 34], and the introduction of vacancies [35, 36] and dopants [37, 38]. These research efforts help reduce the energy barriers for dislocation nucleation and facilitate the dislocation-induced toughening mechanism. Apart from dislocations, complementary deformation mechanisms, including twinning [31, 39, 40], stacking fault formation [31, 32], kink banding [41], microcracking [42], and local atom [43] and vacancy rearrangement [44, 45], have been shown to enhance plasticity and toughness in ceramic materials.

Laser shock peening (LSP) has demonstrated significant potential to enhance strength, wear resistance, and fatigue limit of metallic materials [46–49]. During LSP, a short laser pulse creates high-temperature plasma and a high-pressure shock wave [50], producing localized plastic deformation at extremely high strain rates. Currently, most LSP studies adopt nanosecond laser pulses (ns-LSP), which requires a confining medium (water or glass), leading to a peak shock pressure of ~ 10–20 GPa and significant thermal damage [51, 52]. In contrast, femtosecond laser shock peening, with a laser pulse duration of 200 fs can generate peak shock wave pressures up to hundreds of GPa and significantly reduce thermal damage due to its ultra-high laser intensity and small heat-affected zone [46, 53, 54].

In contrast to the large number of LSP studies on metals, much fewer efforts have been made to treat ceramics with LSP. Prior studies focus primarily on nanosecond LSP (ns-LSP) treatment of SiC [55], Al_2O_3 [56, 57], Si_3N_4 [14], and ZrO_2 [58], which have shown only limited improvements in hardness and indentation fracture resistance after LSP processing. Nonetheless, the effect of fs-LSP on the mechanical properties of ceramics remains unexplored. It remains unknown how fs-LSP would differ from ns-LSP in toughening ceramics. In this regard, this study seeks to advance our understanding of this field by investigating the effects of fs-LSP on the microstructure and mechanical properties of rutile TiO_2 using advanced characterization and computational material science techniques. Our findings demonstrate remarkable toughening effects of hierarchical defects, including vacancies, dislocations, stacking faults, and twins introduced by fs-LSP.

2 | Materials and Methods

2.1 | Fs Laser Shock Peening

The fs-LSP experiments were conducted on (001) single-crystal rutile TiO_2 samples polished by EPI method (99.99%, MTI Corporation) under ambient atmospheric conditions. The surface was ultrasonically cleaned with 99.9% isopropyl alcohol for 5 minutes and subsequently dried on a hot plate at 400°C prior to the laser processing. A Yb:KGW femtosecond laser source (Pharos, Light Conversion) was configured to generate high-energy laser pulses at a central wavelength of 1030 nm with a pulse duration of 165 fs. The laser source was delivering linearly polarized Gaussian-shaped beams at a fixed repetition rate of 3 kHz with a beam diameter of 34 μm at focus and approximately 5 mm before focusing. The laser beam was focused perpendicularly on the sample surface using an *f*-theta lens mounted in the scan head (IntelliScan, ScanLab). The input power of the laser was controlled by a half-wave plate and a polarizer, as shown in Figure 1.

During laser processing, the sample was mounted on a linear translational stage that could move along the vertical direction. A uniform scanning strategy was implemented by maintaining equal spacing between two consecutive pulses in both lateral and transverse directions. The overlapping ratio was predetermined as shown in Table 1, and the corresponding scanning speed was calculated based on the overlapping ratio. The overlapping ratio ($\phi(\%)$) and the hatching distance (D) are expressed as:

$$\phi = \left(1 - \frac{v}{w_o f}\right) \times 100 \quad (1)$$

$$D = \left(1 - \frac{\phi}{100}\right) \times w_0 \quad (2)$$

where, v is the scanning speed, w_0 is the spot diameter, and f is the repetition rate. The fs-LSP system configurations and other parameters are included in Figure 1a. Three TiO_2 samples, referred to as LSP TiO_2-x (x = 1, 2, 3), were processed using different laser parameter combinations, which are shown in Figures 1b–d and Table 1.

2.2 | Microstructure Characterization

The surface roughness and morphology of the as-LSP-processed TiO_2 (AP LSP TiO_2) samples were examined using an Olympus LEXT Optical Profiler and the Hitachi SU5000 scanning electron microscope using BSE detectors under low vacuum mode. AP LSP TiO_2 samples were slightly polished using 1000-grit SiC paper to remove nanoporous layers. Raman backscattering spectroscopy was performed on both AP and polished LSP TiO_2 samples with a Horiba LabRAM HR Evolution confocal microscope equipped with an 800 mm focal length spectrograph and an air-cooled (-60°C) back-illuminated deep-depleted CCD detector. A 100 mW, 532 nm laser (no neutral density filter was used), 50× magnification objective, and 1800 groves/mm diffraction grating were used in the measurements. Spectra were corrected by the pre-recorded instrument-specific intensity correction system (ICS). X-ray diffraction (XRD) measurements were conducted on SmartLab automated multipurpose X-ray diffractometer using a Cu Kα source.

Surface oxygen vacancies in rutile TiO_2 were evaluated using X-ray photoelectron spectroscopy (XPS) on a PHI 5000 VersaProbe III system (Physical Electronics, ULVAC-PHI) equipped with a monochromatic Al Kα X-ray source (1486.7 eV). The measurements were conducted at room temperature with an X-ray power of 50 W and an incidence angle of 90°. The XPS spectra were collected using three sweeps with a pass energy of 69 eV. The analysis chamber was maintained at a ~10^{-7} Pa, and a low-energy electron

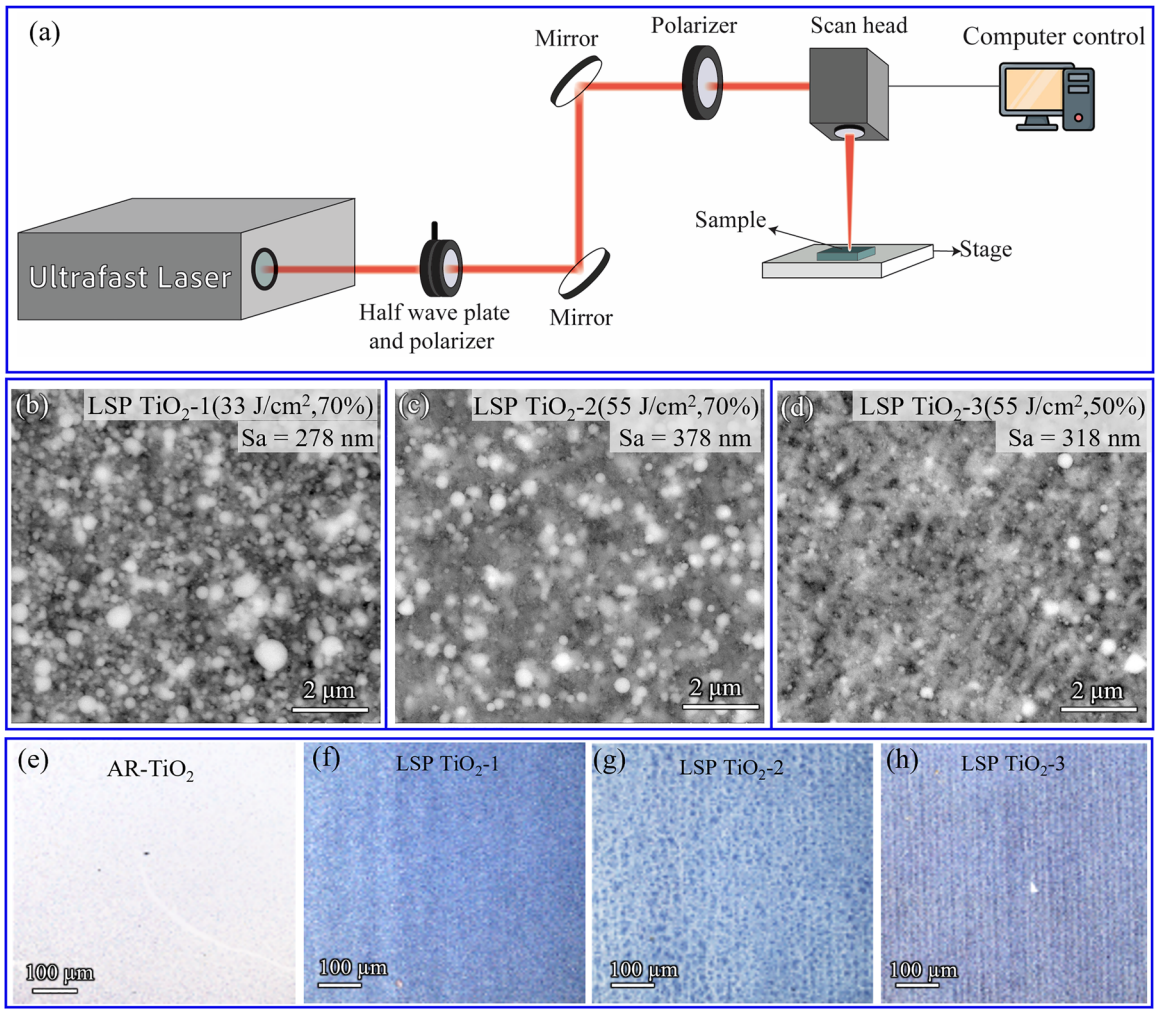

FIGURE 1 | (a) A schematic illustrating the ultrafast laser shock peening system. (b–d) Back-scattered-electron scanning electron microscopy (BSE-SEM) images showing the surface morphologies of TiO_2 samples processed by fs-LSP. Surface roughness values (Sa) and corresponding laser processing parameters for each sample are included. (e–h) Optical images collected by an Olympus LEXT optical profiler showing the color and surface morphology of as-received (AR) TiO_2 and LSP-processed TiO_2 samples.

TABLE 1 | Laser shock peening parameters.

Repetition rate (kHz)	Sample	Peak fluence (J/cm^2)	Average fluence (J/cm^2)	Overlapping ratio (%)	Hatch distance (μm)	Scanning speed (mm/s)
3	LSP TiO_2-1	66	33	70	10.2	30.6
	LSP TiO_2-2	110	55	50	10.2	51.0
	LSP TiO_2-3	110	55	70	17.0	30.6

gun was used for dual-beam charge neutralization during data acquisition. The X-ray beam spot size was 200 μm, with a raster area of 500 × 500 μm^2. Prior to spectral acquisition, all samples were subjected to Ar^+ sputtering cleaning at an accelerating voltage of 2 kV for 12 s. All binding energies were calibrated using the C 1s peak at 284.8 eV. The XPS spectra and binding energy profiles were analyzed using the CasaXPS software. It should be aware that Ar^+ sputtering may induce partial surface reduction in TiO_2. Therefore, identical sputtering conditions were applied to all samples to enable a consistent comparative analysis.

The Thermo Fisher Helios G4 UX dual-beam SEM, equipped with a focused ion beam (FIB) and an Omniprobe manipulator, was used to fabricate a 100-nm-thick sample from LSP TiO_2-1 using a Ga^+ ion source. Microstructure and crystal orientation of the LSP TiO_2 were examined using transmission electron microscope (TEM), scanning transmission electron microscopy (STEM), and pression electron diffraction (PED) experiments on a FEI Talos 200X TEM equipped with Nano Megas ASTAR system. Inverse pole figure orientation (IPF) maps and kernel average misorientation (KAM) map were extracted from the PED dataset via the EDAX/TSL OIM analysis software.

2.3 | Vickers Indentation

Microhardness and indentation fracture resistance (K_{IFR}) of as-received (AR) and polished LSP TiO_2 samples were measured using Vickers hardness tests with loads ranging from 0.05 Kilogram force (kgf) to 1 kgf and a dwell time of 15 s. To probe the penetration depth of LSP-affected layer, Vickers hardness tests were also performed on the cross-section of LSP TiO_2-2 sample at varying distances to the LSP-treated surface using a load of 0.05 kgf. Indents on TiO_2 samples were examined using the JCM-7000 NeoScope Benchtop SEM using BSE detectors. Diagonal length (d) of indents and crack length statistics were measured using ImageJ software. The indentation depth (h) of the indent is estimated to be 1/7 d, considering the square-based pyramid tip used in our Vickers hardness tests. At least 8–10 indents were conducted under each load to ensure data reproducibility.

2.4 | Atomistic Simulation

Atomistic simulations are used to estimate the single-crystal elastic constants and generalized stacking fault energy (GSFE) of pristine rutile TiO_2 and TiO_2 with different oxygen vacancy concentrations (1–5 at.%) using the SevenNet [59] universal ML interatomic potential. The stiffness tensor, C_{ij}[60], is calculated using the stress-strain method [61] at 300 K via the molecular dynamics simulation. Effective elastic constants were obtained for the six independent components $C_{11}, C_{12}, C_{13}, C_{33}, C_{44}$, and C_{66} on a 2058-atom supercell.

Voigt average bulk modulus (K_V), shear modulus (G_V), and elastic modulus (E_V) were calculated based on simulated effective elastic constants ($\boldsymbol{C}^*_{ij}$) using the following Equations (3)–(5) [62]:

$$K_V = \frac{1}{9}\left[2\left(C^*_{11} + C^*_{12}\right) + 4C^*_{13} + C^*_{33}\right] \tag{3}$$

$$G_V = \frac{1}{15}\left[C^*_{11} + C^*_{12} + 2C^*_{33} - 4C^*_{13} + 6C^*_{44} + 3C^*_{66}\right] \tag{4}$$

$$E_V = \frac{9K_V G_V}{3K_V + G_V} \tag{5}$$

where effective elastic constants ($\boldsymbol{C}^*_{ij}$) are calculated from the raw elastic constants ($\boldsymbol{C}_{ij}$) using the following equations:

$$C^*_{11} = \frac{C_{11} + C_{22}}{2}, \quad C^*_{12} = C_{12} \tag{6}$$

$$C^*_{13} = \frac{C_{13} + C_{23}}{2}, \quad C^*_{33} = C_{33} \tag{7}$$

$$C^*_{44} = \frac{C_{44} + C_{55}}{2}, \quad C^*_{66} = C_{66} \tag{8}$$

where the raw elastic constants (C_{ij}) describe the configuration-specific elastic response of a material and reflect the actual symmetry and local disorder of the simulated or measured structure. Effective elastic constants (C^*_{ij}) obtained by averaging and enforcing an appropriate macroscopic symmetry represent the continuum-scale elastic behavior of the material.

The GSFE provides an essential landscape for assessing mechanical stability and slip behavior. The unstable stacking-fault energy (γ_{usf}) is the local maximum on the GSFE curve and quantifies the barrier to nucleating a partial slip/dislocation. For rutile TiO_2, we used the molecular static simulation to compute GSFE at 0 K on the (101) plane using a supercell-oriented $x \parallel [010]$, $y \parallel [\bar{1}01]$, and $z \parallel [101]$. The GSFE curve was generated by rigidly translating the upper half of the crystal relative to the lower half along the in-plane $[\bar{1}01]$ direction over one periodic repeat (one Burgers-vector period), relaxing atoms along the plane normal direction at each increment under in-plane periodic boundary conditions. Our GSFE supercell contains 4116 atoms.

3 | Results

3.1 | SEM and Optical Images

Figures 1b–d show SEM images for the AP LSP TiO_2 samples. The surface roughness increases from 30 nm (AR TiO_2) to 278–378 nm after LSP treatment. The LSP-induced surface roughening likely stems from the formation of nanopores and nanoparticles on LSP-processed TiO_2. Surface morphologies vary among the three LSP TiO_2 samples, exhibiting different sizes and density of nanoparticles. LSP TiO_2-3 has the least number of nanoparticles on its surface (Figure 1d). Notably, low-magnification optical images in Figures 1e–h show significant blackening on surfaces of LSP-processed TiO_2 samples, implying introduction of oxygen vacancies.

3.2 | Raman Spectroscopy

Figure 2 summarizes the Raman spectroscopy profiles for the AR (unprocessed), AP LSP, and polished LSP TiO_2 samples. Compared to AR counterparts, A_{1g}, E_g, B_{1g}, and R peaks shift to lower wavelength numbers in LSP TiO_2 samples. For instance, the position of A_{1g} peak shifts from 612 cm^{-1} (AR TiO_2) to 603 cm^{-1}(AP LSP TiO_2-1), 607 cm^{-1}(AP LSP TiO_2-2), and 601 cm^{-1}(AP LSP TiO_2-3) after LSP treatments. The left (red) peak shifts in the Raman spectra of TiO_2 strongly indicate weakened Ti–O bonds and oxygen vacancies [2, 63]. The removal of the surface nanoporous layer leads to smaller red-shift values in polished LSP TiO_2-1 and LSP TiO_2-3 samples. Compared to AR TiO_2, the multi-phonon peaks (226–242 cm^{-1}) in LSP TiO_2 samples are notably stronger and broader, which suggests the formation of high-density microstructural defects and local microstructural modifications induced by fs-LSP [64]. The oxygen-deficient Magnéli phase was not detected in LSP-processed TiO_2 samples.

3.3 | X-ray Diffraction

AR rutile TiO_2 samples after fs-LSP treatments exhibit surface roughening with the formation of nanopores (Figure 4a) and nanoparticles (Figures 1b–d). The thickness of these nanoporous layers is below 500 nm (Figure 4a), which is comparable to the surface roughness (Sa = 278–378 nm) of LSP-treated surfaces. Noticeably, the LSP TiO_2-3 sample surface (Figure 1d) has a significantly lower density of nanoparticles than the other two samples (Figures 1b,c). Raman spectroscopy results for AP LSP TiO_2 samples in Figure 2 show anatase peaks in LSP TiO_2-1 (Figure 2f) and LSP TiO_2-2 (Figure 2d), but not in LSP TiO_2-3.

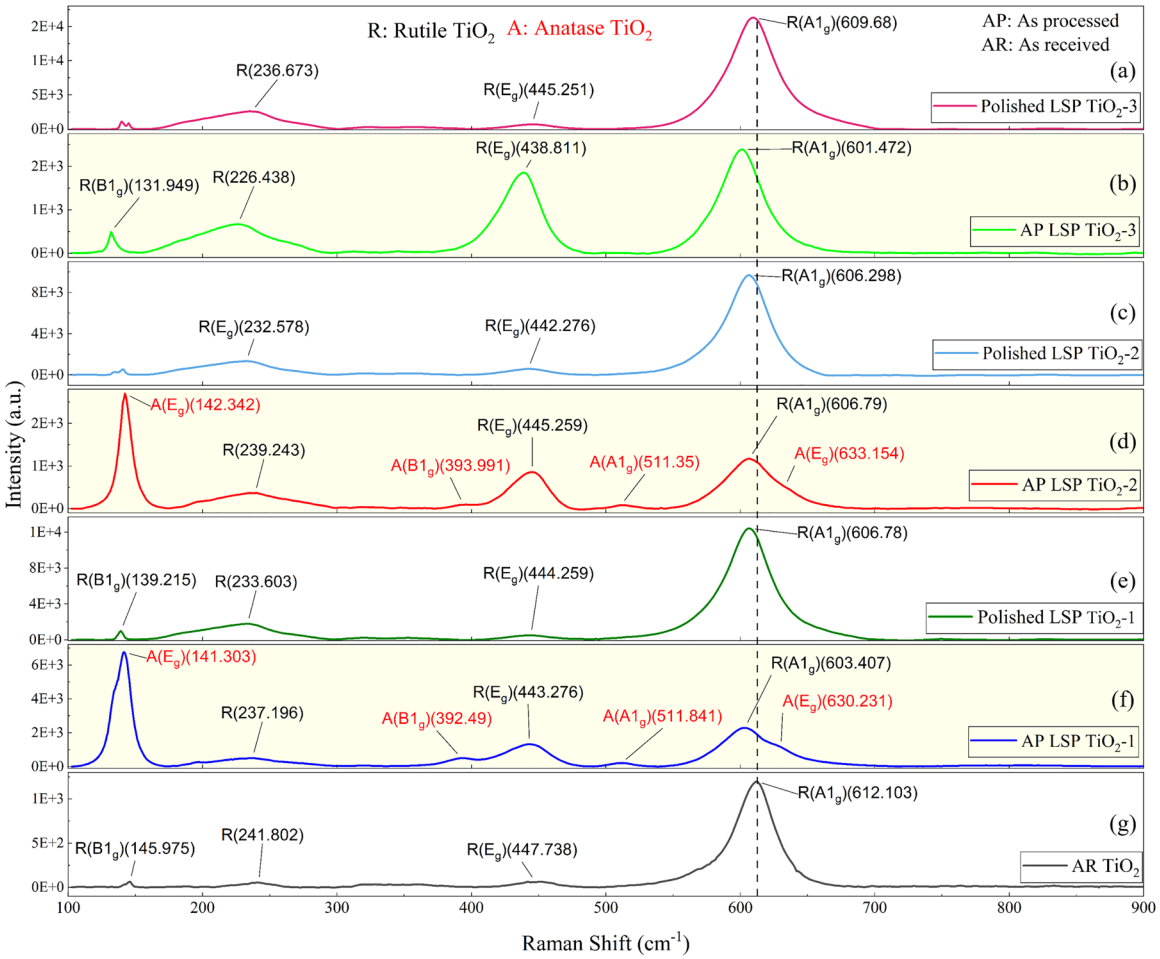

FIGURE 2 | Raman spectra for the as-received (AR), as-processed (AP) LSP TiO_2, and polished LSP TiO_2 samples.

SEM (Figures 1b–d) and Raman spectroscopy results (Figure 2) imply that nanoparticles are likely to be anatase TiO_2 induced by fs-LSP. XRD scans (Figure 3a) show a shift of out-of-plane orientation from <001> in AR TiO_2 to <101> in AP LSP TiO_2 samples. Interestingly, the out-of-plane orientation of the polished LSP TiO_2 samples is <001> (Figure 3a).

Refined XRD scans show the peak broadening and left peak shifts of the (002) peaks in polished LSP TiO_2 samples (Figure 3b). The full width at half maximum (FWHM) for the AR TiO_2 is 0.03°, which is significantly smaller than those of the LSP TiO_2 samples (0.10–0.18°), suggesting the existence of LSP-induced defects and variations in micro strains. Moreover, 0.01–0.05° lower 2θ angle peak shifts were observed in the rutile (002) peaks of LSP TiO_2 samples, indicating the tensile out-of-plane strain and compressive in-plane strain. The corresponding in-plane residual stress (σ_r) can be estimated:

$$\sigma_r = -E' \frac{C_{33}}{2C_{13}} \left(\frac{\sin\theta_0 - \sin\theta_1}{\sin\theta_1} \right) \quad (9)$$

where, C_{ij} is elastic constant, θ_0 and θ_1 are Bragg's angles before and after LSP treatment, E' is the biaxial modulus [65] and can be estimated as $E' = C_{11} + C_{12} - 2(C_{13})^2/C_{33}$. The E' is estimated to be ~ 307.8 GPa using our calculated effective elastic constants as shown in Table 3. Based on this corrected anisotropic equation, the estimated in-plane compressive residual stress is ~-183 MPa (LSP TiO_2-1), −61 MPa (LSP TiO_2-2), and −306 MPa (LSP TiO_2-3), where negative sign indicates compressive residual stress. Notably, these residual stress values should be interpreted as an order-of-magnitude estimation rather than accurate direct measurements because the measured peak position may also be affected by fs-LSP-induced micro strain, defects, and peak broadening [66]. The local microstrain and defect formation could change the shape, width, symmetry of XRD peaks, making the peak position sensitive to fitting procedure. In addition, conventional XRD $\sin^2\psi$ stress analysis is not applicable to our single-crystal TiO_2 sample because tilting the sample will cause the loss of selected diffraction condition [67]. Raman spectroscopy stress analysis is suitable for measuring residual stress in LSP TiO_2 as Raman peak shifts in TiO_2 are strongly correlated with formation of oxygen vacancies [68] as shown in Figure 2. More accurate residual stress measurement might be achieved via X-ray synchrotron diffraction in our prospective study [69].

3.4 | X-ray Photoelectron Spectroscopy (XPS)

Figure 3c shows the Ti 2p XPS spectra of AR and LSP-treated TiO_2 after polishing. Clear Ti^{3+} (Ti2p) features are observed in LSP-treated TiO_2 samples, whereas the Ti^{3+} (Ti2p) signal is negligible in the AR TiO_2 samples prior to the LSP treatments.

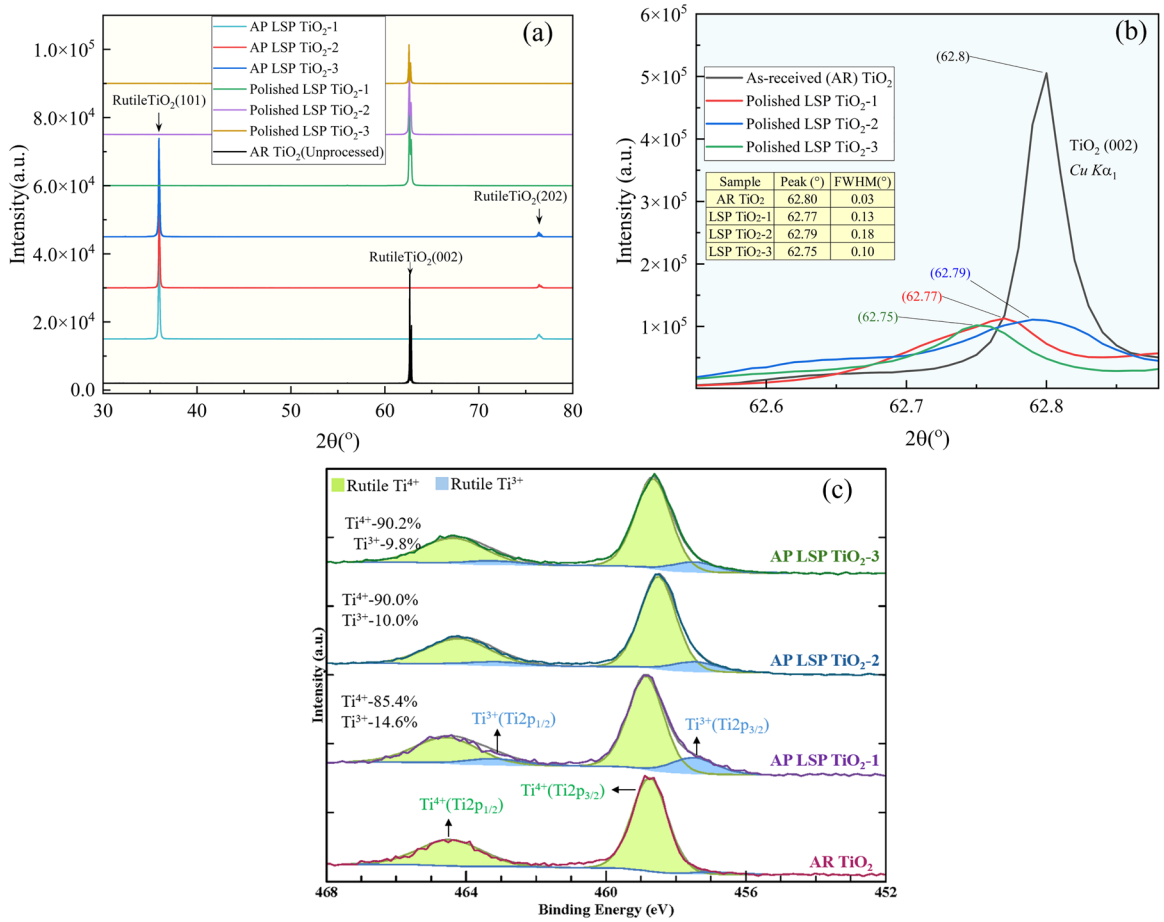

FIGURE 3 | (a) X-ray profiles of the LSP-processed TiO_2 in the AP and polished state. (b) Magnified XRD profiles showing the position and profiles of the (002) peaks in AR and polished LSP TiO_2 samples. (c) Ti 2p XPS spectra of the as-received (AR) and LSP-treated TiO_2 samples after polishing.

The presence of Ti^{3+} suggests partial reduction of TiO_2 and is commonly associated with the formation of oxygen-vacancy-related defects [70, 71]. Based on the fitted Ti^{3+} fractions, the atomic fraction of Ti^{3+} is 14.6 at. %, 10.0% and 9.8 at. % for the LSP-treated samples, respectively. Assuming that each oxygen vacancy contributes to electrons that reduce two Ti^{4+} ions to Ti^{3+} ions [72], the corresponding oxygen vacancy concentrations are estimated to be approximately 7.3 at.%, 5.0 at.% and 4.9 at.% in the near-surface (top 5–10 nm) region of the LSP-treated TiO_2 samples [73], respectively. Noticeably, because XPS probes only the near-surface region (top 5–10 nm) [74], the oxygen vacancy concentrations calculated from Ti^{3+} fractions should be interpreted as surface-layer values. The overall oxygen vacancy concentration over the full LSP-affected depth is likely to be lower.

3.5 | Scanning/Transmission Electron Microscopy (S/TEM) Analysis

Figures 4 and 5 show the microstructure, defects, and crystal orientation of the LSP TiO_2-1 after the fs-LSP treatment. Several defects, including horizontal stacking fault ribbons on {101} (red arrows in Figure 4a), inclined stacking fault ribbons on {011} (white arrows in Figures 4a–c), slip band packets (yellow arrows in Figures 4a–c), dislocation arrays (blue arrows in Figure 3), and nanotwins (Figures 5a,b), were introduced by LSP treatments. The diffraction patterns in Figures 4a,b), HRTEM images (Figures 4c,d) with streak-like FFT patterns, and the inverse pole figure (IPF) orientation map (Figures 5a–c) confirm the formation of high-density stacking faults and nano twins. Notably, stacking faults, twins, and dislocation slip packets in LSP-processed TiO_2 intersect and connect with others, forming defect networks. Stacking faults and slip packets are dominant defects induced by LSP. Accumulation of geometrically necessary dislocations (GNDs) and formation of slip packets has led to a Kernel average misorientation (KAM) of 0.28° in LSP-processed TiO_2 (Figure 5d) The GND density (ρ_{GND}) can be estimated based on the local misorientation using the strain gradient model [75, 76]:

$$\rho_{GND} = \frac{\theta_{KAM}}{x_s b} \tag{10}$$

where, θ_{KAM} is the *KAM* misorientation angle in radians, x_s is the acquisition step size (10 nm) of the PED experiment, and b is the magnitude of the Burgers vectors for partial or full dislocations in rutile TiO_2 (0.27–0.55 nm). The estimated GND density is 0.86–$1.79 \times 10^{15}/m^2$.

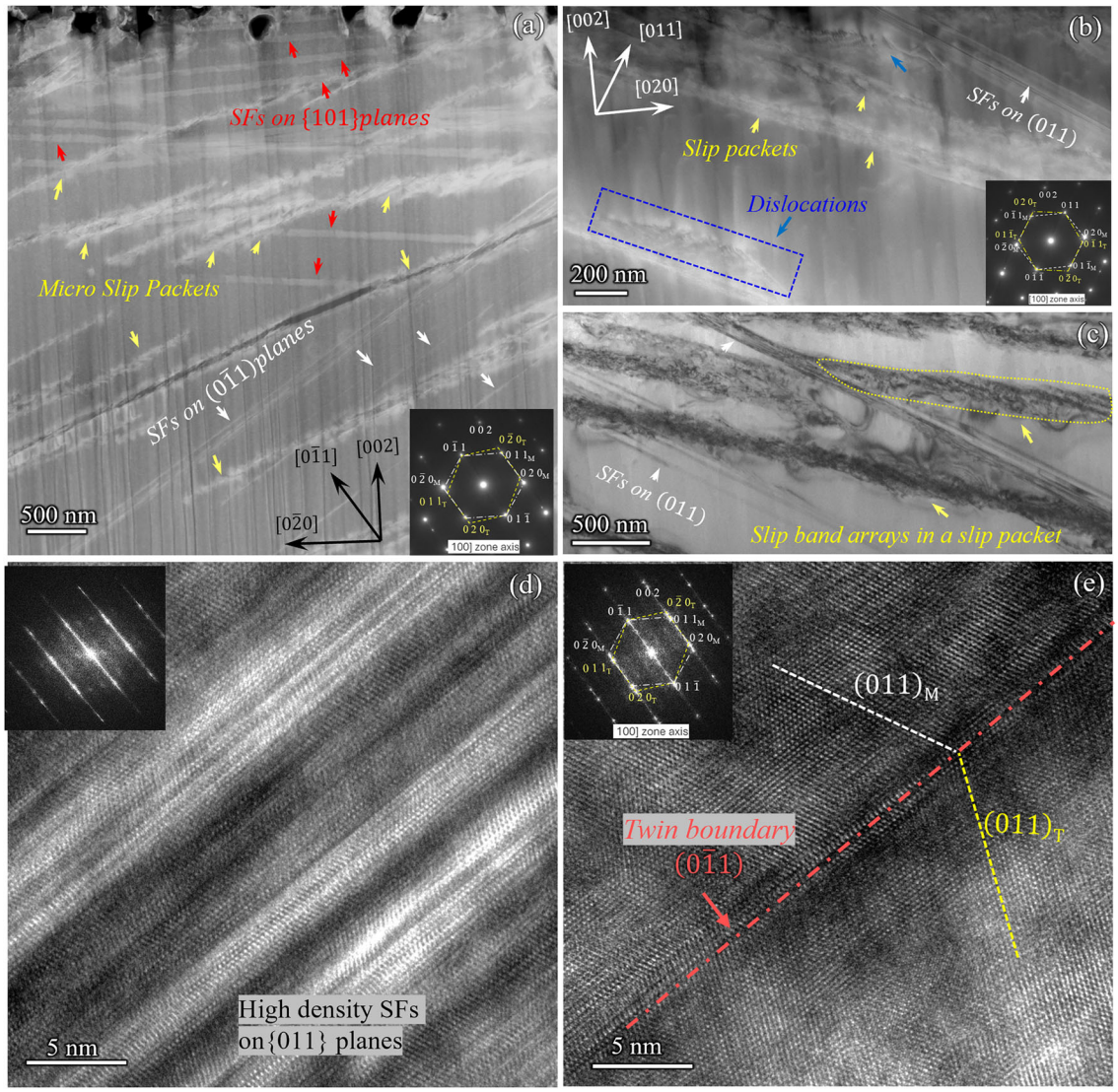

FIGURE 4 | Microstructure of the LSP TiO_2-1 sample. (a) A high-angle-annular dark field (HAADF) scanning transmission electron microscopy (STEM) image shows several slip packets, stacking faults (SFs) ribbons on {101} and {011} planes. (b) A HAADF STEM image shows dislocation arrays, slip packets/bands, and SFs. (c) A bright-field TEM (BF-TEM) image shows arrays of slip bands within slip packets. (d) A high-resolution TEM (HRTEM) image and fast Fourier transform (FFT) patterns show a twin boundary decorated with SFs in TiO_2. (e) A HRTEM image with FFT pattern demonstrates the existence of stacking faults.

3.6 | Vickers Hardness and Indentation Fracture Resistance (K_{IFR})

The Vickers hardness (H_V) of TiO_2 samples in GPa can be estimated as:

$$H_V = 0.018186 \times \frac{F}{d^2} \tag{11}$$

where, F is the applied load in N, d is the average diagonal length in micrometers (μm). The Vickers hardness values (GPa) of TiO_2 samples are plotted as a function of indentation depth in Figure 7a. Hardness of all TiO_2 samples decreases with increasing indentation depth and plateaus at a depth of ~ 4.5 μm, which is known as the indentation size effect governed by GND activity in the case of strain gradient. LSP TiO_2 samples show an average of ~7.8% hardness increases in comparison to the AR TiO_2 sample within the current indentation depth range (< 7 μm). The top 2-μm indentation depth has more obvious hardening, especially in the LSP TiO_2-2 sample. Figure 7b shows the cross-sectional hardness of LSP TiO_2-2 sample as a function of distance to the LSP-treated sample surface. As shown in Figure 7b, the cross-sectional hardness slightly decreases with increasing distance from the treated surface and reaches a plateau at a depth of approximately 55 μm. The average hardness within the top 55 μm region is 12.9 ± 0.6 GPa, whereas the average hardness below 55 μm is 11.2 ± 0.4 GPa. The plateau hardness is nearly identical to that of the AR TiO_2 measured along the in-plane direction. Considering the strengthening effect induced by LSP treatment, it is reasonable to conclude that the LSP-modified layer extends to approximately 55 μm beneath the treated surface.

Figures 6a–d show indents collected under an applied load of 1 kgf on AR and LSP TiO_2 samples. Cracks were nucleating from the apexes and sides of a single indent in AR TiO_2 samples.

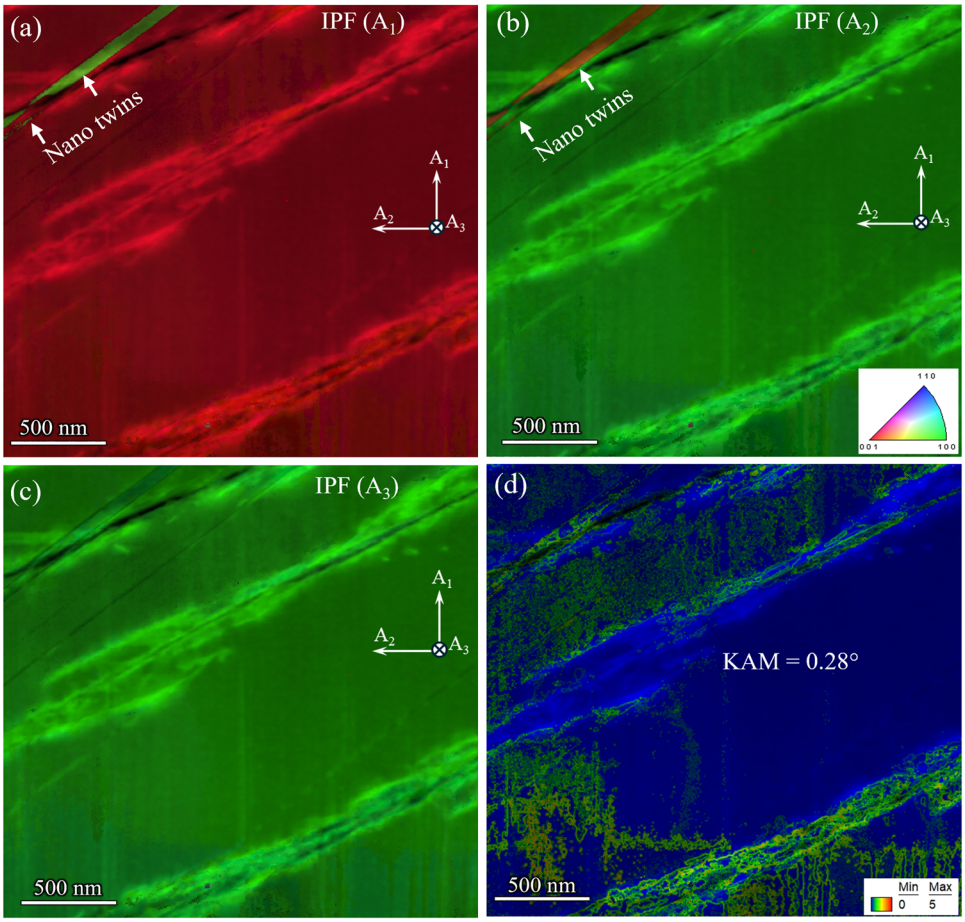

FIGURE 5 | (a–c) Inverse pole figure (IPF) orientation maps of LSP TiO_2-1 specimen shown from different axis. (d) The Kernel average misorientation (KAM) map shows an average misorientation of 0.28°.

Our SEM images and statistics in Figure 6 show that the crack density and length are significantly reduced in LSP TiO_2. The mean crack length to the indent center (c) for those cracks nucleating from the indent apexes is about 91.3 ± 7.3 μm, 43.1 ± 7.2 μm, 45.0 ± 5.9 μm, and 48.6 ± 5.8 μm in AR, LSP TiO_2-1, LSP TiO_2-2, and LSP TiO_2-3, respectively. On average, there are ~20–30 cracks per indent in AR TiO_2, whereas LSP TiO_2 samples have 10–15 cracks per indent. Moreover, most cracks in unprocessed AR TiO_2 are straight. In contrast, many cracks in LSP TiO_2 samples are wavy, caused by crack deflection and branching. The indentation fracture resistance (K_{IFR}) can be estimated using the Anstis equation [77, 78], and the Lankford equation [79] respectively:

$$K_{IFR} = 0.016 \frac{F}{c^{1.5}} \left(\frac{E}{H_V} \right)^{0.5} \quad (Anstis) \tag{12}$$

$$K_{IFR} = 0.0782 \left(H_V a^{0.5} \right) \left(\frac{E}{H_V} \right)^{0.4} \left(\frac{c}{a} \right)^{-1.56} \quad (Lankford) \tag{13}$$

where, F is the applied load of Vickers indentation in N, a is the half of the diagonal length of indent, c is the project length of radial cracks measured from the crack tip to the center of an indent, H_V is the Vickers hardness in GPa, and E is the Young's modulus of Rutile TiO_2 (270 GPa). It is worth noting that only radial cracks nucleating from indent corners are considered for crack length statistics. Notably, cracks in LSP-processed TiO_2 deviated from ideal median cracks with crack deflection and crack branching observed. One commonly used empirical method to distinguish median/half-penny cracks from Palmqvist cracks is based on the c/a ratio [80, 81]: cracks are generally classified as median cracks when c/a > 2.5, whereas cracks with smaller values c/a < 2.5 are more likely to be Palmqvist-type cracks. As shown in Table 2, the cracks in the AR TiO_2 are mostly median cracks, whereas Palmqvist-type cracks are more prevalent in the LSP-treated TiO_2 samples. Compared with the Anstis model, the Lankford model is less restricted to a single idealized crack type and has been applied to both median/half-penny and Palmqvist crack systems [80, 82]. According to the Anstis model, the estimated K_{IFR} values (MPa$\sqrt{m}$) of LSP TiO_2 samples are 8.2 ± 2.1 (LSP TiO_2-1), 7.7 ±1.6 (LSP TiO_2-2), and 6.8 ±1.3 (LSP TiO_2-3), which are 2.5–3.0 times the K_{IFR} of unprocessed AR TiO_2 (2.8 ± 0.3 MPa $\sqrt{m}$). The indentation fracture resistance values of LSP TiO_2 estimated by Lankford model are slightly lower than those derived from Anstis model as shown in Table 2. Both Anstis and Lankford models show pronounced increase in indentation fracture resistance. It should be pointed out that K_{IFR} derived from Anstis and Lankford equations should be treated as apparent indentation fracture resistance rather than standard plane-strain fracture toughness.

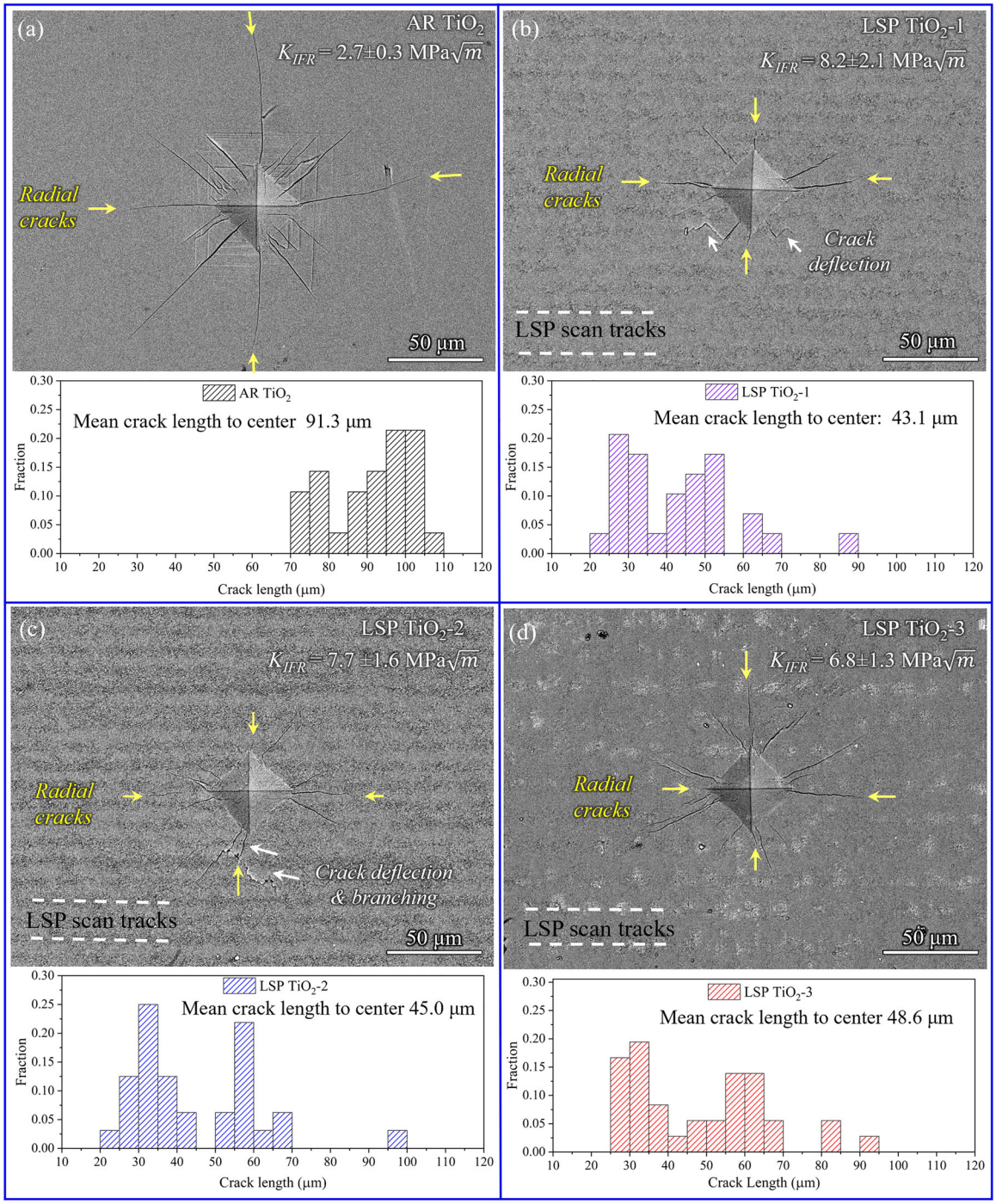

FIGURE 6 | SEM images with corresponding crack length statistics of Vickers hardness indents on AR TiO_2 (a) and LSP TiO_2 (b–d) surfaces. Radial cracks are labeled with yellow arrows, and the LSP scan tracks are outlined with white dash lines. Surface damage layers from LSP were gently removed prior to the Vickers hardness tests.

4 | Discussion

4.1 | Microstructure Evolutions Induced by Fs Laser Shock Peening

Our post-LSP characterization revealed different microstructural defects and compressive residual stress within the LSP-affected layer in LSP-processed TiO_2. As shown in Figure 7b, the estimated depth of this LSP-affected layer is approximately 55 μm beneath the surface, which is shallower than typical affected depth (hundreds of μm) of nanosecond LSP ceramics [14, 15, 55–58, 83]. This is mainly due to the ultra-short laser pulse duration (165 fs) of our femtosecond laser source. Although femtosecond laser source can generate ultra-high transient pressure of hundreds of GPa near the surface [53], the associated pressure pulse duration is short at the order of 100–200 fs, which is much smaller than those in conventional nanosecond LSP process [51]. As a result, shock stress attenuates rapidly with increasing depth and falls below

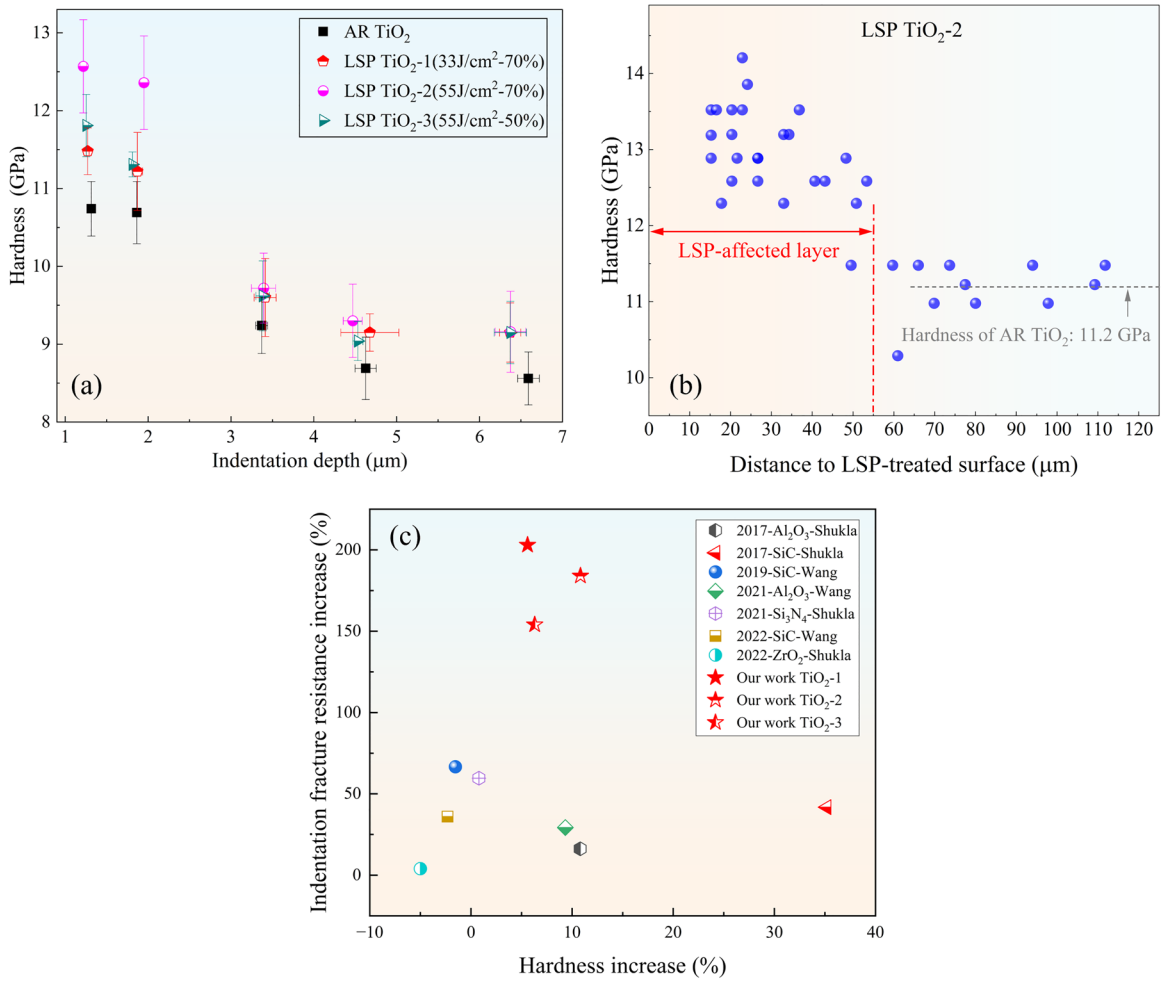

FIGURE 7 | (a) Vickers hardness of AR and LSP TiO_2 samples collected at different indentation depths using loads ranging from 0.05 kgf to 1 kgf. (b) Vickers hardness of the LSP TiO_2-2 sample on its cross-section along the in-plane <010> direction using the applied load of 0.05 kgf. (c) Comparison of toughening and strengthening effects of LSP in ceramic materials from different studies [14, 15, 55–58, 83]. Indentation fracture resistance data points from literatures and this study (Anstis model) were all collected via Vickers indentation method.

TABLE 2 | Estimated indentation fracture resistance K_{IFR} with crack length parameters in TiO_2 samples.

Sample	c (μm)	c/a	Crack type	K_{IFR} (Anstis) MPa $\sqrt{m}$	K_{IFR} (Lankford) MPa $\sqrt{m}$
AR	91.3 ± 7.3	4.0	Median	2.8 ± 0.3	3.0 ± 0.3
LSP TiO_2-1	43.1 ± 7.2	1.9	Palmqvist	8.2 ± 2.1	6.7 ± 1.2
LSP TiO_2-2	45.0 ± 5.9	2.0	Palmqvist	7.7 ± 1.6	6.5 ± 0.9
LSP TiO_2-3	48.6 ± 5.8	2.0	Palmqvist	6.8 ± 1.3	6.0 ± 0.8

the critical stress threshold to activate plastic deformation and defects generation. Consequently, the LSP-induced hardening and microstructural modification are confined to the top 55 μm.

Our post-LSP characterization results show the formation of hierarchical defects including oxygen vacancies, dislocations, stacking faults and twins. It assumed that the ultrahigh-transient pressure/temperature and strain rate facilitate the formation of complex defects in LSP-treated TiO_2 specimens. The formation of oxygen vacancies after fs-LSP can be attributed to the highly non-equilibrium laser–matter interactions [50] near the TiO_2 surface. The intense femtosecond laser irradiation can induce Ti–O bond breaking, surface ablation [84, 85], and preferential oxygen loss, leading to local reduction of TiO_2. The removal of lattice oxygen produces oxygen vacancies and releases excess electrons, which can reduce neighboring Ti^{4+} to Ti^{3+} [72]. Moreover, the ultrashort pulse duration and rapid cooling may further limit the re-incorporation of oxygen vacancy, allowing these non-equilibrium defects to be retained near the surface.

Apart from vacancies, fs-LSP has introduced abundant dislocations and dislocation structures, with a GND density of 0.86–1.79 $\times 10^{15}/m^2$. Dislocation slip band packets consisting of array of micro slip bands are frequently observed in TiO_2. It is assumed that nucleation of dislocations is induced by high peak stress (up to hundreds of GPa), high temperature and high strain rate during the fs-LSP treatment. Li et al. [53] demonstrated that femtosecond laser shock peening can produce extremely strong shock wave with pressure of hundreds of GPa near the surface. Our fs-LSP treatment used the same type of femtosecond laser source and a comparable laser fluence range to that reported by Li et al. Although this pressure is not directly equivalent to the resolved shear stress on a specific slip system, it can generate large deviatoric stress and resolved shear stress that surpass the compressive yield strength (3–4 GPa) and critical resolved shear stress (CRSS) in rutile TiO_2.

Without considering kink pair formation and migration, the dependence dislocation density (ρ_d) and dislocation velocity (v_d) on applied shear stress (τ^*) and temperature (T) can be described by using this Arrhenius-type equation [19, 86, 87]:

$$\dot{\varepsilon} = m\rho_d v_d b = \dot{\varepsilon}_0 \exp\left(-\frac{\Delta H - V\tau^*}{k_B T}\right) \tag{14}$$

where, $\dot{\varepsilon}$ is the strain rate, $\dot{\varepsilon}_0$ is the pre-exponential constant, m is the effective Schmid factor, k_B is the Boltzmann constant, T is the deformation temperature in Kelvin, and ΔH is the activation enthalpy, which is usually below 0.1 eV for face-centered cubic (FCC) metals, and 0.3–0.8 eV for body-centered cubic (BCC) metals, and 3–10 eV for strongly ionic/covalent ceramics including Al_2O_3 and TiO_2 and SiC. As described in Equation (14), increasing applied shear stress τ^* and deformation temperature can facilitate dislocation nucleation and multiplication in TiO_2. Under LSP, this condition is met by extremely high transient stress and local temperature rise, which can reduce the activation barrier for dislocation motion and promote rapid dislocation nucleation and multiplication. Interestingly, dislocations in TiO_2 generated by fs-LSP treatments are mostly located in slip packets/bands and dislocation arrays rather than being randomly distributed, indicating localized plasticity in LSP-processed TiO_2.

High-density stacking faults are also observed in our LSP TiO_2. The formation of these stacking faults is attributed to the gliding ½ <011> and ½ <101> partial dislocations on {011} and {101} planes [88, 89]. These partial dislocations may originate from dissociation of full dislocations assisted by high local stress and high strain rate during LSP. Gliding of partial dislocations on adjacent {011} and {101} planes can lead to formation of twins. In addition, the formation of stacking faults and twins is further promoted by ultra-high strain rate. As a complementary deformation mechanism, deformation twinning can be activated when dislocation alone is not sufficient to accommodate plasticity at ultrahigh strain rate [90].

4.2 | Toughening Mechanisms in LSP-Processed TiO_2

As shown in Figure 7c, our fs-LSP treatment produces a significant increase in indentation fracture resistance, outperforming prior ns-LSP studies [14, 15, 55–58, 83]. The remarkable enhancement in the K_{IFR} of LSP TiO_2 might stem from synergetic and cooperative effect of compressive residual stress and multi-dimensional defects, including oxygen vacancies, dislocations, stacking faults, and twins.

4.2.1 | Impact of Compressive Residual Stress

Introducing compressive residual stress is an effective toughening method that can suppress crack opening and crack propagation by reducing the stress intensity at the crack tips. Compared to metals, introducing residual stress into ceramics without breaking their integrity is challenging. Prior studies show that nanosecond LSP can impart near-surface residual stress in Al_2O_3 [15], SiC [83], and Si_3N_4 [14], with magnitudes ranging from −94 to −1000 MPa.

In a layer with uniform residual stress near the surface, the stress intensity (K_I) of a straight crack is [91]:

$$K_I = K_0^I + 2\left(\frac{l}{\pi}\right)^{0.5} \int_0^w \frac{\sigma_r}{\sqrt{(l^2 - x^2)}} dx \tag{15}$$

where, K_I^0 is the stress intensity without residual stress, l is the Griffith flaw size, x is the depth from the surface, σ_r is the residual stress, and w indicates the thickness of the residual stress layer. In the case of compressive residual stress, where the sign of σ_r is negative, the K_I is smaller than K_I^0. Equation (15) indicates that compressive residual stress can toughen material by reducing the stress intensity ahead of the crack tip. Compared to recent nanosecond LSP studies, the estimated residual stress (−61 to −306 MPa) is similar or smaller, with potentially a smaller residual stress layer thickness (w) due to the shallower penetration depth (~55 μm) of the fs laser beam. According to Equation (15), residual stress is unlikely to play a dominant role in toughening LSP-processed TiO_2. Therefore, the more prominent toughening contribution should be ascribed to microstructural defects, including oxygen vacancies, dislocations, twins, and stacking faults.

4.2.2 | Influence of Oxygen Vacancies

Our Raman results (Figure 2), XPS results (Figure 3c), and the optical images (Figures 1e–h) have implied the existence of oxygen vacancies in LSP-processed TiO_2 samples. Oxygen vacancies in our LSP-processed TiO_2 samples can lead to significant increase in toughness by promoting dislocation activity and the formation of stacking faults. Oxygen vacancies play a critical role in affecting the nucleation and mobility of dislocations in rutile TiO_2 by modifying local bonding [92], local charge distribution [93], and lattice stiffness [94]. At the low to intermediate vacancy concentration, oxygen vacancies weaken the Ti–O bonds and soften the lattice of rutile TiO_2 as evidenced by red shift of A_{1g} and E_g peaks of rutile TiO_2 (Figure 2) [63]. Our atomistic simulation results (Figures 8a,b, Table 3) concur with this argument by showing decrease of elastic constants, bulk modulus (K_V), shear modulus (G_V), and Young's modulus (E_V) with increasing oxygen concentration up to 5 at.%. Accordingly, it is expected that critical

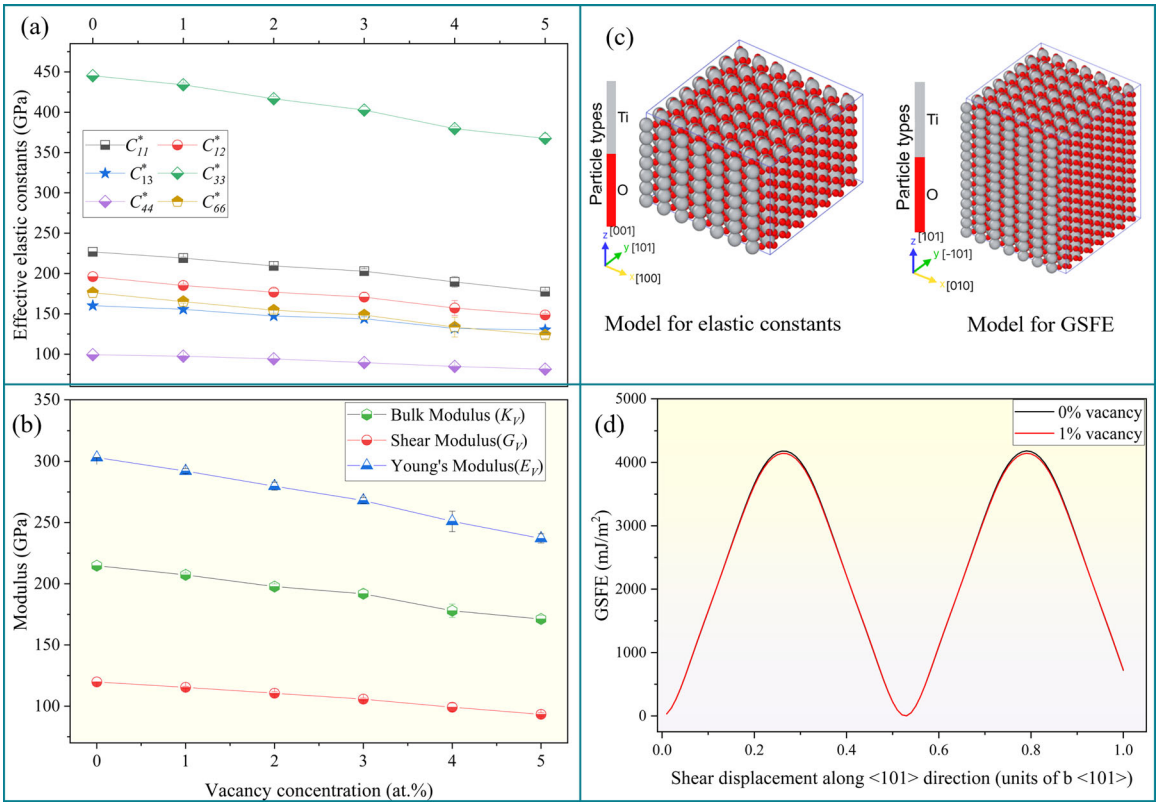

FIGURE 8 | (a and b) Effective elastic constants (C^*_{ij}), bulk modulus (K_V), shear modulus (G_V), and Young's modulus (E_V), evolving with oxygen vacancy concentrations in TiO_2 calculated by molecular dynamic simulation. (c) Atomistic simulation model configurations for calculating elastic constants and generalized stacking fault energy (GSFE). (d) GSFE profiles for pristine rutile TiO_2 and rutile TiO_2 with 1 at.% oxygen vacancies calculated by static molecular simulations.

TABLE 3 | Effective elastic constants (C^*_{ij}) obtained from atomistic simulation.

Vacancy (%)	C^*_{11} (GPa)	C^*_{12}(GPa)	C^*_{13}(GPa)	C^*_{33}(GPa)	C^*_{44}(GPa)	C^*_{66}(GPa)
0	226.93 ± 0.01	196.21 ± 0.01	160.26 ± 0.00	445.19 ± 0.01	99.33 ± 0.00	176.38 ± 0.00
1	219.19 ± 1.43	185.26 ± 1.59	155.67 ± 1.10	434.03 ± 2.24	97.59 ± 0.58	165.34 ± 2.02
2	209.52 ± 0.99	176.98 ± 4.61	147.37 ± 1.25	416.71 ± 2.57	94.25 ± 0.36	154.56 ± 3.74
3	202.99 ± 3.02	170.79 ± 5.37	144.10 ± 2.29	402.72 ± 4.50	89.63 ± 0.47	148.64 ± 0.75
4	189.71 ± 6.61	157.28 ± 9.33	131.96 ± 3.78	379.60 ± 2.55	84.81 ± 1.30	133.55 ± 12.35
5	177.47 ± 1.91	148.65 ± 2.15	130.25 ± 3.18	367.51 ± 5.96	81.44 ± 0.95	123.93 ± 4.23

resolved shear stress for dislocation nucleation will be reduced in surface regions with oxygen deficiency.

In addition, oxygen vacancies and associated Ti^{3+} can partially neutralize the charged dislocation cores, leading to relaxed and wider dislocation cores. The Peierls–Nabarro stress (τ_p) for dislocation gliding is expressed as [86, 87]:

$$\tau_p = \frac{2G}{1-\nu} \exp\left(-\frac{2\pi\omega}{b}\right) \tag{16}$$

where, G is the shear modulus, ν is the Poisson's ratio, b is the dislocation Burgers vector magnitude and ω is the dislocation core width. As Equation (16) indicates, oxygen vacancy can reduce τ_p by reducing shear modulus and increasing dislocation core with, thereby enhancing dislocation mobility in TiO_2. Yang et al. [35] reported higher dislocation density in vacancy-rich TiO_2 under nanoindentation. It should be noticed that higher oxygen vacancy concentration might lead to formation of vacancy clusters that can pin dislocations and reduce the mobility of dislocation.

Moreover, oxygen vacancy could affect stacking fault energy (SFE) of TiO_2 depending on their atomic scale distribution as demonstrated by Li et al. [95] in flash sintered TiO_2. Our atomistic simulation results in Figure 8d suggests that impact of oxygen vacancy on the SFE of TiO_2 is negligible compared to its impact on elastic constants (Figure 8a). Adding 1 at.% oxygen vacancies

slightly lowers the unstable stacking fault energy (γ_{usf}) of TiO_2 from 4181 to 4143 mJ /m^2 while maintain similar stable SFE (γ_{sf}) (17.6–52.0 vs. 16.0–50.2 mJ/m^2). The ultra-high γ_{usf} indicates that partial dislocation nucleation in rutile TiO_2 is strongly hindered, whereas the very low γ_{usf} suggests that stacking faults are energetically stable once form. Extreme conditions in fs-LSP process, including ultra-high local stresses and strain rates can overcome nucleation barrier and enable the formation of stacking faults and twins. Oxygen-vacancy-induced reductions in both γ_{usf} and γ_{sf} could slightly facilitate their initiation and stabilization.

LSP-induced oxygen vacancies may indirectly enhance the fracture resistance of TiO_2 by lowering the energy barrier for dislocation nucleation, increasing dislocation mobility, and facilitating the formation of stacking faults and twins. The toughening contributions associated with dislocations, twins, and stacking faults are discussed in detail in the following subsections.

4.2.3 | Toughening Effect of Dislocations and Dislocation Structures

Dislocations introduced by fs-LSP treatments are likely to toughen the TiO_2 in the following aspects. First, stress fields associated with slip packets and dislocation arrays can shield the crack and reduce the effective stress intensity ahead of crack tip. Stress fields generated by dislocation structures, such as slip packets, slip bands and arrays, are deemed to be more long-ranged than those from random dislocations, leading to stronger crack tip shielding effect [96–98]. Dislocations included in these dislocation structures have similar orientation and Burgers vectors, incurring superimposition of elastic field rather than cancelling out in randomly distributed dislocations [97, 99]. Second, emission of dislocations from a crack tip can dissipate elastic energy and generate back stress that can reduce stress intensity by blunting crack tip [100]. The dislocation activity ahead of crack tips is promoted by lowered critical resolved shear stress for dislocation nucleation and smaller Peierls–Nabarro stress for gliding at crack tips in LSP TiO_2 samples with oxygen vacancies. Additionally, the work associated with dislocation glide within the plastic zone ahead of the crack tip can dissipate elastic strain energy and contribute to toughening [100]. Third, LSP-generated slip packets/bands can toughen the TiO_2 by deflecting crack tips, as demonstrated by those wavy crack paths in Figure 6b–d.

4.2.4 | Toughening Contribution of Stacking Faults and Twins

To the best of our knowledge, high-density stacking faults and twins have not been reported in LSP-processed ceramics in prior studies. The extraordinary toughening in LSP TiO_2 sample is likely due to high-density stacking faults and some twin boundaries. Prominent toughening effects from stacking faults and twins have been reported in TiN/TaN [32], CrN [39], SiC [31], and aragonite [22]. Stacking faults and twins can toughen the TiO_2 by cracks deflection/branching, crack shielding, and crack blunting. First, crack tips can be arrested by stacking faults and twin boundaries, and be forced to change their paths, thereby increasing the fracture surface area and energy dissipation [101]. LSP-induced stacking faults and twins can generate crystallographic discontinuities that can interfere with crack propagation, leading to deflection, branching, and arresting of cracks. Second, local stress fields of twin boundaries/stacking faults can toughen TiO_2 via crack tip shielding. As demonstrated in previous studies [102–104], local stress fields can develop near twin boundaries due to deformation incompatibility and elastic anisotropy. Local stress fields of twin boundaries and stacking faults can decrease the stress intensity at the crack tip, resulting in increased fracture toughness. Third, emissions of partial dislocations from crack tips generate local back stress that can reduce stress intensity at the crack tip [31, 105], thereby further toughening the TiO_2. In addition, stacking faults and twins are strong barriers for dislocations. Therefore, dislocations nucleating from crack tips may pile up against stacking faults and twins, leading to greater back stress for crack shielding [97].

4.2.5 | Cooperative Toughening Mechanisms in LSP-treated TiO_2

Overall, the significant increase in the indentation fracture resistance of TiO_2 arises from the synergistic effects of compressive residual stress, oxygen vacancies, dislocation structures, stacking faults, and twins induced by fs-LSP treatment. However, separating the relative contribution of each defect type in the present study is challenging because compressive residual stress, oxygen vacancies, dislocations, twins, and stacking faults are introduced simultaneously during LSP treatment and interact with one another during their formation and subsequent deformation. Therefore, the improved indentation fracture resistance of LSP-processed TiO_2 should be considered the combined result of cooperative toughening mechanisms. Among these mechanisms, oxygen vacancies may indirectly promote defect-mediated toughening by facilitating dislocation nucleation and glide, as well as promoting the formation of twins and stacking faults. Dislocations and dislocation structures can toughen TiO_2 through crack deflection, crack-tip shielding by their stress fields, crack-tip blunting through dislocation emission, and strain-energy dissipation through dislocation glide. Stacking faults and twins can increase the toughness of TiO_2 through crack deflection and branching, crack-tip shielding by local stress fields, and crack-tip blunting through the emission of partial dislocations. Additionally, LSP-induced compressive residual stress may partially offset the tensile opening stress at the crack tip, thereby reducing the effective stress intensity factor. Among these mechanisms, dislocations, slip bands/packets, stacking faults, and twins are expected to provide more dominant toughening contributions. Although the toughened layer is limited to the top tens of micrometers, fs-LSP can potentially improve the damage tolerance of the bulk structure because most failures and cracks initiate from the material surface [106].

4.3 | Reliability and Limitation of Vickers Indentation Fracture Method

Palmqvist first proposed the idea of applying Vickers indentation to determine fracture resistance in the 1950s [107], and it was later applied by Evans and Charles [108] in the 1970s to assess fracture

behavior. This technique has been widely used to study fracture behaviors of brittle material [78, 80, 109–112]. So far, several empirical models have been developed to extract indentation fracture resistance or apparent indentation fracture toughness [78, 79, 108, 110, 113, 114]. This work selected the Anstis equation [77, 78] and the Lankford equation [82] as a comparison. Anstis equation is based median crack model, whereas equation is applicable to both median and Palmqvist cracks [78, 80].

However, as a non-traditional method, Vickers indentation method has some inherent limitations due to limitations for determining the fracture toughness of brittle materials because of the ill-defined crack-arrest condition [109], the formation of multiple cracks, and possible deviations from the ideal crack-geometry assumptions [115]. Therefore, the Vickers indentation method should be treated as an approach for estimating the apparent indentation fracture resistance rather than a rigorous measurement of plane-strain fracture toughness.

In particular, the Anstis equation assumes a well-defined radial/median half-penny crack geometry. However, crack branching and crack deflection were observed in some of the indentation cracks in the LSP-processed TiO_2 samples. Such non-ideal crack morphologies inevitably introduce uncertainty in the measurement of crack length and, consequently, in the calculated indentation fracture resistance [116, 117]. The underlying reason for this issue is the presence of microcracks and the inherent three-dimensional crack structures under high indentation loading. This issue can be minimized by measuring the average microcrack penetration depth, as demonstrated by Moradkhani et al. [118]. Therefore, the measured K_{IFR} values are influenced by measurement conditions and should be interpreted with caution.

In LSP-processed TiO_2 samples, crack morphologies deviate from the standard median/half-penny geometry, resulting in asymmetrical crack morphologies at the four corners of an indent. The asymmetrical crack geometries might arise from the heterogeneous distribution of crystal defects introduced by our LSP scanning strategy. LSP tracks are delineated by horizontal white dashed lines as shown in Figure 6. Accordingly, radial cracks perpendicular to LSP scan tracks are obviously shorter than those aligning parallel with LSP scan tracks. Despite these asymmetries, radical cracks are still visible at most indent corners in the LSP-processed TiO_2 specimens. Branched/deflected cracks were frequently observed in the LSP-processed TiO_2 specimen (Figures 6b–d), which might cause some uncertainties of the calculated K_{IFR}.

In this study, the projected straight-line distance from the indentation center to the visible crack tip was adopted as the crack length(c) in the Anstis equation. For branched cracks, the main crack path was selected for the measurement. We recognize that this projected crack length may be shorter than the actual tortuous crack path, which could lead to an increase in the calculated apparent indentation fracture resistance. However, the number of cracks showing branching or deflection accounts for only approximately 25% – 35% of the total cracks nucleated from the indentation corners. Therefore, although these crack morphologies introduce some uncertainty, they are not expected to change the overall comparative trend. In our future study, 3D reconstruction of the microcrack networks via synchrotron radiation X-ray topography (SR-XRT) [119, 120] or sequential slicing with focused ion beam [121] can be pursued to more accurately capture facture behaviors of brittle ceramics.

In summary, non-ideal crack morphologies introduce uncertainty in defining and measuring the representative crack length. Because the calculated indentation fracture resistance is highly sensitive to crack length, a shorter projected crack length caused by crack deflection, branching, or crack arrest may lead to an overestimation of the apparent toughness. However, our SEM images with corresponding crack length statistics clearly show reduced crack length, branched, and deflected crack tips in LSP-processed TiO_2 specimens (Figure 6). The crack branching and deflection observed in LSP TiO_2 samples suggest the activation of extrinsic toughening mechanisms, including crack-path tortuosity and crack-tip shielding. These mechanisms can increase the energy required for crack propagation and therefore contribute to enhanced resistance to indentation-induced cracking after LSP. In addition, identical and validated indentation conditions [14, 15, 55–58, 83] were applied to all samples, the relative changes in K_{IFR} remain meaningful for comparative evaluation of crack resistance.

5 | Conclusions

This work is one of the first studies exploring the surface toughening of TiO_2 via ultrafast femtosecond laser shock peening treatment (fs-LSP). Compared with limited toughening increase of ns-LSP (< 55%), fs-LSP can toughen the surface rutile of TiO_2 by a factor of two to three, increasing indentation fracture resistance (Anstis model) from 2.8 to 8.2 MPa$\sqrt{m}$. Remarkable toughening effects are attributed to synergetic toughening effects of compressive residual stress and multidimensional defect networks, including vacancy, dislocation structures, stacking faults, twins. Our fs-LSP processing recipes can be expanded to other ceramics, including carbides, nitrides, and oxides. This work provides a cost-effective and scalable approach to significantly toughen the surface of brittle ceramics or refractory metals.

Acknowledgments

Yifan Zhang acknowledges the incentive funding support from the Department of Mechanical Engineering, College of Engineering, Computing, and Applied Sciences (CECAS) at Clemson University. Xin Zhao acknowledges the funding support from the financial support provided for this study by the National Science Foundation (grant no.: 2047000-CMMI). Some of the computing for this project was performed at the OU Supercomputing Center for Education & Research at the University of Oklahoma (OU). Xinghang Zhang and Haiyan Wang acknowledge the support the U.S. Office of Naval Research (contract nos. N00014-17-1-2087 and N00014-22-1-2160). The access to the Life Science Microscopy Facility and the Microscopy Center of the School of Materials Engineering at Purdue University is also acknowledged. We also acknowledge support from Dr. Jianhua Tong and Tianyi Zhou on the access to JCM-7000 NeoScope Benchtop SEM at Department of Materials Science and Engineering, Clemson University.

References

1. W. Rheinheimer, X. L. Phuah, H. Wang, F. Lemke, M. J. Hoffmann, and H. Wang, "The Role of Point Defects and Defect Gradients in Flash

Sintering of Perovskite Oxides," *Acta Materialia* 165 (2019): 398–408, https://doi.org/10.1016/j.actamat.2018.12.007.

2. X. Bi, G. Du, A. Kalam, et al., "Tuning Oxygen Vacancy Content in TiO_2 Nanoparticles to Enhance the Photocatalytic Performance," *Chemical Engineering Science* 234 (2021): 116440, https://doi.org/10.1016/j.ces.2021.116440.

3. J. Zhang, G. Liu, W. Cui, et al., "Plastic Deformation in Silicon Nitride Ceramics via Bond Switching at Coherent Interfaces," *Science* 378, no. 6618 (2022): 371–376, https://doi.org/10.1126/science.abq7490.

4. B. Huang, M. She, J. Chen, et al., "Investigations on the Irradiation Stability at 300°C of the Carbon Black Dispersed Silicon Carbide for Nuclear Applications," *Journal of Nuclear Materials* 605 (2025): 155593, https://doi.org/10.1016/j.jnucmat.2024.155593.

5. B. Kisan, J. Kumar, A. M. Padhan, P. Alagarsamy, and D. Pamu, "Size and Strain Induced Phase Formation and Ferromagnetism in Reduced TiO_2 Powders," *Journal of Physics and Chemistry of Solids* 154, no. March (2021): 110058, https://doi.org/10.1016/j.jpcs.2021.110058.

6. E. E. Benson, E. M. Miller, S. U. Nanayakkara, et al., "Semiconductor-to-Metal Transition in Rutile TiO_2 Induced by Tensile Strain," *Chemistry of Materials* 29, no. 5 (2017): 2173–2179, https://doi.org/10.1021/acs.chemmater.6b04881.

7. M. Höfling, M. Trapp, L. Porz, et al., "Large Plastic Deformability of Bulk Ferroelectric $KNbO_3$ Single Crystals," *Journal of the European Ceramic Society* 41, no. 7 (2021): 4098–4107, https://doi.org/10.1016/j.jeurceramsoc.2021.02.023.

8. P. Gao, S. Yang, R. Ishikawa, et al., "Atomic-scale Measurement of Flexoelectric Polarization at $SrTiO_3$ Dislocations," *Physical Review Letters* 120, no. 26 (2018): 267601, https://doi.org/10.1103/PhysRevLett.120.267601.

9. C. Shen, T. Niu, J. Cho, et al., "In Situ Studies on Temperature-Dependent Deformation Mechanisms of Al_2O_3 Prepared by Spark Plasma Sintering," *Journal of the American Ceramic Society* 108, no. 6 (2025): e19964, https://doi.org/10.1111/jace.19964.

10. C. Shen, J. Li, T. Niu, et al., "Achieving Room Temperature Plasticity in Brittle Ceramics Through Elevated Temperature Preloading," Science Advances 10, no. 16 (2024): 0–9, https://doi.org/10.1126/sciadv.adj4079.

11. N. A. Richter, B. Yang, J. P. Barnard, et al., "Significant Texture and Wear Resistance Improvement of TiN Coatings Using Pulsed DC Magnetron Sputtering," *Applied Surface Science* 635 (2023): 157709, https://doi.org/10.1016/j.apsusc.2023.157709.

12. J. Gan, C. Jiang, Y. Zhang, et al., "Effect of TiN Coating on Suppressing Ce-Fe Interaction Under Irradiation," *Materialia* 38 (2024): 102221, https://doi.org/10.1016/j.mtla.2024.102221.

13. J. Cho, X. L. Phuah, J. Li, et al., "Temperature Effect on Mechanical Response of Flash-sintered ZnO by in-situ Compression Tests," *Acta Materialia* 200 (2020): 699–709, https://doi.org/10.1016/j.actamat.2020.09.029.

14. P. Shukla, X. Shen, R. Allott, et al., "Response of Silicon Nitride Ceramics Subject to Laser Shock Treatment," *Ceramics International* 47, no. 24 (2021): 34538–34553, https://doi.org/10.1016/j.ceramint.2021.08.369.

15. F. Wang, X. Yan, L. Liu, M. Nastasi, Y. Lu, and B. Cui, "Surface Strengthening of Single-crystal Alumina by High-temperature Laser Shock Peening," *Materials Research Letters* 9, no. 3 (2021): 155–161, https://doi.org/10.1080/21663831.2020.1862933.

16. L. Porz, "60 years of Dislocations in Ceramics: A Conceptual Framework for Dislocation Mechanics in Ceramics," *International Journal of Ceramic Engineering & Science* 4, no. 4 (2022): 214–239, https://doi.org/10.1002/ces2.10150.

17. R. O. Ritchie, "The Conflicts Between Strength and Toughness," *Nature Materials* 10, no. 11 (2011): 817–822, https://doi.org/10.1038/nmat3115.

18. M. Li, Y. Shen, K. Luo, et al., "Harnessing Dislocation Motion Using an Electric Field," *Nature Materials* 22, no. 8 (2023): 958–963, https://doi.org/10.1038/s41563-023-01572-7.

19. Y. Kamimura, K. Edagawa, and S. Takeuchi, "Experimental Evaluation of the Peierls Stresses in a Variety of Crystals and Their Relation to the Crystal Structure," *Acta Materialia* 61, no. 1 (2013): 294–309, https://doi.org/10.1016/j.actamat.2012.09.059.

20. Y. Rong, S. Zhao, Q. Zhang, et al., "High-Performance Alumina Composite Ceramics With Brick-and-Mortar Structure Derived From Microsphere," *International Journal of Ceramic Engineering & Science* 7, no. 2 (2025): e70002, https://doi.org/10.1002/ces2.70002.

21. M. Li, G. Zu, Y. Qiao, et al., "Effect of Different TiNi/Ti_2Ni Ratios on the Compressive Properties and Toughening Mechanisms of Biomimetic Brick-and-mortar Structural Composites," *Materials & Design* 260 (2025): 115113, https://doi.org/10.1016/j.matdes.2025.115113.

22. Y. A. Shin, S. Yin, X. Li, et al., "Nanotwin-governed Toughening Mechanism in Hierarchically Structured Biological Materials," *Nature Communications* 7 (2016): 1–10, https://doi.org/10.1038/ncomms10772.

23. C. A. Schmidt, W. O. Nachlas, B. Schneider, et al., "Multiple Twinning in Nacre and Aragonite," *Advanced Functional Materials* 36 (2025): e18248, https://doi.org/10.1002/adfm.202518248.

24. Q. Meng, Q. Zhang, and X. Shi, "Hierarchical Crossed-Lamellar Structure in Conch Shells: Mechanics and Biomimetics," *Journal of the American Ceramic Society* 108 (2025): e20465, https://doi.org/10.1111/jace.20465.

25. V. Ogunjimi, M. A. Sebastian, D. Zhang, et al., "Enhancing Magnetic Pinning by $BaZrO_3$ Nanorods Forming Coherent Interface by Strain-directed Ca-doping in $YBa_2Cu_3O_{7-X}$ Nanocomposite Films," *Superconductor Science and Technology* 34 (2021): 104002, https://doi.org/10.1088/1361-6668/ac1fd3.

26. J. Cho, Q. Li, H. Wang, et al., "High Temperature Deformability of Ductile Flash-sintered Ceramics via in-situ Compression," *Nature Communications* 9, no. 1 (2018): 2063, https://doi.org/10.1038/s41467-018-04333-2.

27. X. Fang, W. Lu, J. Zhang, et al., "Harvesting Room-temperature Plasticity in Ceramics by Mechanically Seeded Dislocations," *Materials Today* 82, no. February (2025): 81–91, https://doi.org/10.1016/j.mattod.2024.11.014.

28. O. Preu, E. Bruder, J. Zhang, W. Lu, and R. Jürgen, "Journal of the European Ceramic Society Damage-tolerant Oxides by Imprint of an Ultra-high Dislocation Density," *Journal of the European Ceramic Society* 45, no. July 2024 (2025): 116969, https://doi.org/10.1016/j.jeurceramsoc.2024.116969.

29. Y. Cui, X. Fang, and W. Lu, Scale-bridging Dislocation Plasticity in MgO at Room Temperature, n.d., 1–51.

30. J. Li, J. Cho, J. Ding, et al., "Nanoscale Stacking Fault–assisted Room Temperature Plasticity in Flash-sintered TiO_2," *Science Advances* 5, no. 9 (2019): 1–10, https://doi.org/10.1126/sciadv.aaw5519.

31. J. Zhao, Z. Xu, Z. Yan, et al., "Stacking Faults Toughened SiC Ceramics Formed by FSPS Induced Grain Deformation," *Journal of the European Ceramic Society* 45, no. 13 (2025): 117499, https://doi.org/10.1016/j.jeurceramsoc.2025.117499.

32. Y. Huang, Z. Chen, M. Meindlhumer, et al., "Harvesting Superior Intrinsic Plasticity in Nitride Ceramics With Negative Stacking Fault Energy," *Acta Materialia* 286, no. December 2024 (2025): 120774, https://doi.org/10.1016/j.actamat.2025.120774.

33. L. R. Dong, J. Zhang, Y. Z. Li, et al., "Borrowed Dislocations for Ductility in Ceramics," *Science* 385, no. 6707 (2024): 422–427, https://doi.org/10.1126/science.adp0559.

34. J. Zhang, G. Liu, W. Cui, et al., "Plastic Deformation in Silicon Nitride Ceramics via Bond Switching at Coherent Interfaces," *Science* 378, no. D (2022): 371–376.

35. B. Yang, N. Richter, H. Li, et al., "Dislocation-enabled Plasticity in Rutile TiO_2−X at Room Temperature," *Nanoscale* 17, no. 35 (2025): 20338–20350, https://doi.org/10.1039/d5nr02684a.

36. X. Fang, K. Ding, S. Janocha, et al., "Nanoscale to Microscale Reversal in Room-temperature Plasticity in $SrTiO_3$ by Tuning Defect Concentration," *Scripta Materialia* 188 (2020): 228–232, https://doi.org/10.1016/j.scriptamat.2020.07.033.

37. M. Li, J. Li, K. Luo, et al., "Opposite Effects of Doping on Nanoindentation Pop-in Phenomena in InAs and Ge Crystals," *Scripta Materialia* 261, no. November 2024 (2025): 1–5, https://doi.org/10.1016/j.scriptamat.2025.116607.

38. X. Liu, R. Wang, J. Zhang, et al., "Doping-dependent Nucleation of Basal Plane Dislocations in 4H-SiC," *Journal of Physics D: Applied Physics* 55, no. 33 (2022): 334002, https://doi.org/10.1088/1361-6463/ac7178.

39. L. Liu, X. An, X. Gu, et al., "Nanotwinned CrN Ceramics With Enhanced Plasticity," *Nature Communications* 16, no. 1 (2025): 1–10, https://doi.org/10.1038/s41467-025-61275-2.

40. S. Yang, T. Guo, X. Yan, K. Gao, and X. Pang, "High-density Twin Boundaries in Transition Metal Nitride Coating With Boron Doping," *Acta Materialia* 255, no. May (2023): 119033, https://doi.org/10.1016/j.actamat.2023.119033.

41. H. J. Rathod, T. Ouisse, M. Radovic, and A. Srivastava, "Room Temperature Crack-healing in an Atomically Layered Ternary Carbide," *Science Advances* 7, no. 33 (2021): eabg2549, https://doi.org/10.1126/sciadv.abg2549.

42. O. Gavalda-Diaz, E. Saiz, J. Chevalier, and F. Bouville, "Toughening of Ceramics and Ceramic Composites Through Microstructure Engineering: A Review," *International Materials Reviews* 70, no. 1 (2025): 3–30, https://doi.org/10.1177/09506608241308337.

43. E. J. Frankberg, A. Lambai, J. Zhang, et al., "Exceptional Microscale Plasticity in Amorphous Aluminum Oxide at Room Temperature," *Advanced Materials* 35, no. 46 (2023): 1–14, https://doi.org/10.1002/adma.202303142.

44. P. Li, J. Li, Q. Feng, et al., "Unveiling High Ductility in Boron Carbide Crystal at Room Temperature," *Science Advances* 11, no. 15 (2025): eadr4648, https://doi.org/10.1126/sciadv.adr4648.

45. Z. Chen, Y. Huang, N. Koutná, et al., "Large Mechanical Properties Enhancement in Ceramics Through Vacancy-mediated Unit Cell Disturbance," *Nature Communications* 14, no. 1 (2023): 1–11, https://doi.org/10.1038/s41467-023-44060-x.

46. C. Zhang, Y. Dong, and C. Ye, "Recent Developments and Novel Applications of Laser Shock Peening: A Review," *Advanced Engineering Materials* 23, no. 7 (2021): 1–24, https://doi.org/10.1002/adem.202001216.

47. R. Sundar, P. Ganesh, R. K. Gupta, et al., "Laser Shock Peening and Its Applications: A Review," *Lasers in Manufacturing and Materials Processing* 6 (2019): 424–463, https://doi.org/10.1007/s40516-019-00098-8.

48. X. Yan, F. Wang, L. Deng, et al., "Effect of Laser Shock Peening on the Microstructures and Properties of Oxide-Dispersion-Strengthened Austenitic Steels," *Advanced Engineering Materials* 20, no. 3 (2018): 1–8, https://doi.org/10.1002/adem.201700641.

49. W. Dai, J. Shi, D. Song, et al., "Laser Shock Peening Optimized Microstructure Stabilizes Compressive Residual Stress to Improve Fatigue Performance of High-strength Aluminum Alloy Hole Structure," *Journal of Materials Science & Technology* 246 (2026): 98–115, https://doi.org/10.1016/j.jmst.2025.01.045.

50. X. Jia and X. Zhao, "Numerical Study of Material Decomposition in Ultrafast Laser Interaction With Metals," *Applied Surface Science* 463, no. July 2018 (2019): 781–790, https://doi.org/10.1016/j.apsusc.2018.08.225.

51. M. Jia, Y. Wang, J. Yue, et al., "Recent Progress in Laser Shock Peening: Mechanism, Laser Systems and Development Prospects," *Surfaces and Interfaces* 44, no. December 2023 (2024): 103757, https://doi.org/10.1016/j.surfin.2023.103757.

52. A. Cunha, R. O. Giacomelli, J. Kaufman, J. Brajer, and T. S. Pereira, "An Overview on Laser Shock Peening Process: From Science to Industrial Applications," in 2021 SBFoton International Optics and Photonics Conference (SBFoton IOPC), Sao Carlos, Brazil, 2021, 1–6, https://doi.org/10.1109/SBFotonIOPC50774.2021.9461929.

53. Y. Li, Z. Ren, X. Jia, et al., "The Effects of the Confining Medium and Protective Layer During Femtosecond Laser Shock Peening," *Manufacturing Letters* 27, no. 2021 (2021): 26–30, https://doi.org/10.1016/j.mfglet.2020.11.006.

54. Y. Lian, J. Sun, Z. Zhang, G. Lin, Z. Chen, and Y. Yuan, "Thermo-mechanical Response and Strengthening Effect of Femtosecond Laser-irradiated CoCrFeNi High-entropy Alloy Films," *Surface and Coatings Technology* 483, no. April (2024): 130756, https://doi.org/10.1016/j.surfcoat.2024.130756.

55. P. Shukla, S. Nath, G. Wang, X. Shen, and J. Lawrence, "Surface Property Modifications of Silicon Carbide Ceramic Following Laser Shock Peening," *Journal of the European Ceramic Society* 37, no. 9 (2017): 3027–3038, https://doi.org/10.1016/j.jeurceramsoc.2017.03.005.

56. F. Wang, C. Zhang, Y. Lu, M. Nastasi, and B. Cui, "Laser Shock Processing of Polycrystalline Alumina Ceramics," *Journal of the American Ceramic Society* 100, no. 3 (2017): 911–919, https://doi.org/10.1111/jace.14630.

57. P. Shukla, S. Robertson, H. Wu, et al., "Surface Engineering Alumina Armour Ceramics With Laser Shock Peening," *Materials & Design* 134 (2017): 523–538, https://doi.org/10.1016/j.matdes.2017.08.066.

58. P. Shukla, V. Zhang, X. Shen, V. M. Villapún, S. Cox, and P. Swanson, "Biocompatibility and Surface Integrity of Zirconia Ceramics Treated by Laser-plasma Driven Shock-waves," *Recent Progress in Materials* 04, no. 04 (2022): 1–44, https://doi.org/10.21926/rpm.2204025.

59. Y. Park, J. Kim, S. Hwang, and S. Han, "Scalable Parallel Algorithm for Graph Neural Network Interatomic Potentials in Molecular Dynamics Simulations," *Journal of Chemical Theory and Computation* 20, no. 11 (2024): 4857–4868, https://doi.org/10.1021/acs.jctc.4c00190.

60. W.-R. Jian, S. Xu, and I. J. Beyerlein, "On the Significance of Model Design in Atomistic Calculations of the Peierls Stress in Nb," *Computational Materials Science* 188 (2021): 110150, https://doi.org/10.1016/j.commatsci.2020.110150.

61. S. Xu, Y. Su, W.-R. Jian, and I. J. Beyerlein, "Local Slip Resistances in Equal-molar MoNbTi Multi-principal Element Alloy," *Acta Materialia* 202 (2021): 68–79, https://doi.org/10.1016/j.actamat.2020.10.042.

62. R. Hill, "The Elastic Behaviour of a Crystalline Aggregate," *Proceedings of the Physical Society Section A* 65, no. 5 (1952): 349–354, https://doi.org/10.1088/0370-1298/65/5/307.

63. B. Kisan, J. Kumar, A. M. Padhan, P. Alagarsamy, and D. Pamu, "Size and Strain Induced Phase Formation and Ferromagnetism in Reduced TiO_2 Powders," *Journal of Physics and Chemistry of Solids* 154 (2021): 110058, https://doi.org/10.1016/j.jpcs.2021.110058.

64. T. Lan, X. Tang, and B. Fultz, "Phonon Anharmonicity of Rutile TiO_2 Studied by Raman Spectrometry and Molecular Dynamics Simulations," *Physical Review B* 85, no. 9 (2012): 94305, https://doi.org/10.1103/PhysRevB.85.094305.

65. R. Knepper and S. P. Baker, "Coefficient of Thermal Expansion and Biaxial Elastic Modulus of β Phase Tantalum Thin Films," *Applied Physics Letters* 90, no. 18 (2007): 181908, https://doi.org/10.1063/1.2734468.

66. M. E. Fitzpatrick, A. T. Fry, P. Holdway, F. A. Kandil, J. Shackleton, and L. Suominen, Determination of Residual Stresses by X-ray Diffraction, 2005.

67. A. Sarmast, J. Schubnell, J. Preußner, M. Hinterstein, and E. Carl, "Residual Stress Analysis in Industrial Parts: A Comprehensive Comparison of XRD Methods," *Journal of Materials Science* 58, no. 44 (2023): 16905–16929, https://doi.org/10.1007/s10853-023-09069-z.

68. J. A. Benavides-Guerrero, L. F. Gerlein, C. Trudeau, D. Banerjee, X. Guo, and S. G. Cloutier, "Synthesis of Vacancy-rich Titania Particles Suitable for the Additive Manufacturing of Ceramics," *Scientific Reports* 12, no. 1 (2022): 1–11, https://doi.org/10.1038/s41598-022-19824-y.

69. A. S. Gill, Z. Zhou, U. Lienert, et al., "High Spatial Resolution, High Energy Synchrotron X-ray Diffraction Characterization of Residual Strains and Stresses in Laser Shock Peened Inconel 718SPF Alloy," *Journal of Applied Physics* 111, no. 8 (2012): 084904, https://doi.org/10.1063/1.3702890.

70. B. Santara, P. K. Giri, K. Imakita, and M. Fujii, "Evidence of Oxygen Vacancy Induced Room Temperature Ferromagnetism in Solvothermally Synthesized Undoped TiO_2 Nanoribbons," *Nanoscale* 5, no. 12 (2013): 5476, https://doi.org/10.1039/c3nr00799e.

71. B. Bharti, S. Kumar, H.-N. Lee, and R. Kumar, "Formation of Oxygen Vacancies and Ti^{3+} state in TiO_2 Thin Film and Enhanced Optical Properties by Air Plasma Treatment," *Scientific Reports* 6, no. 1 (2016): 32355, https://doi.org/10.1038/srep32355.

72. K. Yang, Y. Dai, B. Huang, and Y. P. Feng, "Density-functional Characterization of Antiferromagnetism in Oxygen-deficient Anatase and Rutile TiO_2," *Physical Review B* 81, no. 3 (2010): 33202, https://doi.org/10.1103/PhysRevB.81.033202.

73. J. Wang, D. N. Mueller, and E. J. Crumlin, "Recommended Strategies for Quantifying Oxygen Vacancies With X-ray Photoelectron Spectroscopy," *Journal of the European Ceramic Society* 44, no. 15 (2024): 116709, https://doi.org/10.1016/j.jeurceramsoc.2024.116709.

74. D. R. Baer, K. Artyushkova, C. Richard Brundle, et al., "Practical Guides for X-ray Photoelectron Spectroscopy: First Steps in Planning, Conducting, and Reporting XPS Measurements," *Journal of Vacuum Science & Technology A: Vacuum, Surfaces, and Films* 37, no. 3 (2019): 031401, https://doi.org/10.1116/1.5065501.

75. M. Calcagnotto, D. Ponge, E. Demir, and D. Raabe, "Orientation Gradients and Geometrically Necessary Dislocations in Ultrafine Grained Dual-phase Steels Studied by 2D and 3D EBSD," *Materials Science and Engineering: A* 527, no. 10–11 (2010): 2738–2746, https://doi.org/10.1016/j.msea.2010.01.004.

76. Y. Zhang, T. J. Nizolek, L. Capolungo, N. Li, J. S. Carpenter, and R. J. McCabe, "Strong Interfaces: The Key to High Strength in Nano Metallic Laminates," *Acta Materialia* 280 (2024): 120298, https://doi.org/10.1016/j.actamat.2024.120298.

77. G. R. Anstis, P. Chantikul, B. R. Lawn, and D. B. Marshall, "A Critical Evaluation of Indentation Techniques for Measuring Fracture Toughness: I, Direct Crack Measurements," *Journal of the American Ceramic Society* 64, no. 9 (1981): 533–538, https://doi.org/10.1111/j.1151-2916.1981.tb10320.x.

78. A. Moradkhani, V. Panahizadeh, and M. Hoseinpour, "Indentation Fracture Resistance of Brittle Materials Using Irregular Cracks: A Review," *Heliyon* 9, no. 9 (2023): e19361, https://doi.org/10.1016/j.heliyon.2023.e19361.

79. M. T. Laugier, "New Formula for Indentation Toughness in Ceramics," *Journal of Materials Science Letters* 6, no. 3 (1987): 355–356, https://doi.org/10.1007/BF01729352.

80. D. Ćorić, M. Majić Renjo, and L. Ćurković, "Vickers Indentation Fracture Toughness of Y-TZP Dental Ceramics," *International Journal of Refractory Metals & Hard Materials* 64 (2017): 14–19, https://doi.org/10.1016/j.ijrmhm.2016.12.016.

81. C. B. Ponton and R. D. Rawlings, "Vickers Indentation Fracture Toughness Test Part 1 Review of Literature and Formulation of Standardised Indentation Toughness Equations," *Materials Science and Technology* 5, no. 9 (1989): 865–872, https://doi.org/10.1179/mst.1989.5.9.865.

82. J. Lankford, "Indentation Microfracture in the Palmqvist Crack Regime: Implications for Fracture Toughness Evaluation by the Indentation Method," *Journal of Materials Science Letters* 1, no. 11 (1982): 493–495, https://doi.org/10.1007/BF00721938.

83. F. Wang, X. Yan, C. Zhang, et al., "Localized Plasticity in Silicon Carbide Ceramics Induced by Laser Shock Processing," *Materialia* 6, no. October 2018 (2019): 100265, https://doi.org/10.1016/j.mtla.2019.100265.

84. X. Zhao and Y. C. Shin, "Femtosecond Laser Ablation of Aluminum in Vacuum and Air at High Laser Intensity," *Applied Surface Science* 283 (2013): 94–99, https://doi.org/10.1016/j.apsusc.2013.06.037.

85. X. Zhao and Y. C. Shin, "Ablation Enhancement of Silicon by Ultrashort Double-pulse Laser Ablation," *Applied Physics Letters* 105, no. 11 (2014): 111907, https://doi.org/10.1063/1.4896350.

86. D. Hull and D. J. Bacon, *Introduction to Dislocations* (Elsevier, 2011).

87. U. Messerschmidt, *Dislocation Dynamics During Plastic Deformation* (Springer Science & Business Media, 2010).

88. K. H. G. Ashbee, R. E. Smallman, and G. K. Williamson, "Stacking Faults and Dislocations in Titanium Dioxide, With Special Reference to Non-stoichiometry," *Proceedings of the Royal Society of London Series A, Mathematical and Physical Sciences* 276, no. 1367 (1963): 542–552.

89. X. Zheng, S. Zheng, J. Wang, et al., "Twinning and Sequential Kinking in Lamellar Ti-6Al-4 V Alloy," *Acta Materialia* 181 (2019): 479–490, https://doi.org/10.1016/j.actamat.2019.10.010.

90. F. Zhao, L. Wang, D. Fan, et al., "Macrodeformation Twins in Single-Crystal Aluminum," *Physical Review Letters* 116, no. 7 (2016): 1–5, https://doi.org/10.1103/PhysRevLett.116.075501.

91. B. Lawn, *Fracture of Brittle Solids* (Cambridge University Press, 1993), 194, https://doi.org/10.1017/CBO9780511623127.

92. E. Cho, S. Han, H. S. Ahn, K. R. Lee, S. K. Kim, and C. S. Hwang, "First-principles Study of Point Defects in Rutile $TiO_{2-}X$," *Physical Review B* 73, no. 19 (2006): 193202, https://doi.org/10.1103/PhysRevB.73.193202.

93. G. C. Vásquez, S. Z. Karazhanov, D. Maestre, A. Cremades, J. Piqueras, and S. E. Foss, "Oxygen Vacancy Related Distortions in Rutile TiO_2 Nanoparticles: A Combined Experimental and Theoretical Study," *Physical Review B* 94, no. 23 (2016): 235209, https://doi.org/10.1103/PhysRevB.94.235209.

94. F. T. Geldasa and F. B. Dejene, "Effects of S Doping and Oxygen Vacancy on the Physical Properties of Rutile TiO_2 for Photocatalysis Applications Based on Density Functional Theory Study," *Materials* 18, no. 8 (2025): 1688, https://doi.org/10.3390/ma18081688.

95. J. Li, J. Cho, J. Ding, et al., "Nanoscale Stacking Fault–assisted Room Temperature Plasticity in Flash-sintered TiO_2," *Science Advances* 5, no. 9 (2019): 1–9, https://doi.org/10.1126/sciadv.aaw5519.

96. N. Narita, K. Higashida, T. Torii, and S. Miyaki, "Crack-tip Shielding by Dislocations and Fracture Toughness in NaCl Crystals," *Materials Transactions, JIM* 30, no. 11 (1989): 895–907, https://doi.org/10.2320/matertrans1989.30.895.

97. R. Thomson, "Physics of Fracture," in *Solid State Physics* (Elsevier, 1986), 1–129.

98. J. R. Rice and R. Thomson, "Ductile versus Brittle Behaviour of Crystals," *Philosophical Magazine: A Journal of Theoretical, Experimental and Applied Physics* 29, no. 1 (1974): 73–97.

99. O. Preuß, E. Bruder, J. Zhang, W. Lu, J. Rödel, and X. Fang, "Damage-tolerant Oxides by Imprint of an Ultra-high Dislocation Density," *Journal of the European Ceramic Society* 45, no. 2 (2025): 116969.

100. L. L. Fischer and G. E. Beltz, "The Effect of Crack Blunting on the Competition Between Dislocation Nucleation and Cleavage," *Journal of the Mechanics and Physics of Solids* 49, no. 3 (2001): 635–654, https://doi.org/10.1016/S0022-5096(00)00042-9.

101. X. Li, S. Yin, S. H. Oh, and H. Gao, "Hardening and Toughening Mechanisms in Nanotwinned Ceramics," *Scripta Materialia* 133 (2017): 105–112, https://doi.org/10.1016/j.scriptamat.2017.02.003.

102. S. Pfeiffer and M. F.-X. Wagner, "Elastic Deformation of Twinned Microstructures," *Proceedings of the Royal Society A: Mathematical, Physical and Engineering Sciences* 473, no. 2204 (2017): 20170330.

103. T. W. J. Kwok, T. P. Mcauliffe, A. K. Ackerman, et al., "The Mechanism of Twin Thickening and the Elastic Strain state of TWIP Steel Nanotwins," *Materials Science and Engineering: A* 873, no. April (2023): 145005, https://doi.org/10.1016/j.msea.2023.145005.

104. B. Leu, M. A. Kumar, P. F. Rottmann, K. J. Hemker, and I. J. Beyerlein, "Micromechanical Fields Associated With Irregular Deformation Twins

in Magnesium," *Journal of Materials Engineering and Performance* 32, no. 6 (2023): 2688–2699, https://doi.org/10.1007/s11665-022-07196-3.

105. M. Huang and Z. Li, "Dislocation Emission Criterion From a Blunt Crack Tip," *Journal of the Mechanics and Physics of Solids* 52, no. 9 (2004): 1991–2003, https://doi.org/10.1016/j.jmps.2004.03.003.

106. J. C. Stinville, M. A. Charpagne, A. Cervellon, et al., "On the Origins of Fatigue Strength in Crystalline Metallic Materials," *Science* 377, no. 6610 (2022): 1065–1071, https://doi.org/10.1126/science.abn0392.

107. S. Palmqvist, Indentation Hardness and Fracture Toughness in Single Crystal, 1957.

108. A. G. EVans and E. A. Charles, "Fracture Toughness Determinations by Indentation," *Journal of the American Ceramic Society* 59, no. 7–8 (1976): 371–372, https://doi.org/10.1111/j.1151-2916.1976.tb10991.x.

109. J. J. Kruzic, D. K. Kim, K. J. Koester, and R. O. Ritchie, "Indentation Techniques for Evaluating the Fracture Toughness of Biomaterials and Hard Tissues," *Journal of the Mechanical Behavior of Biomedical Materials* 2, no. 4 (2009): 384–395, https://doi.org/10.1016/j.jmbbm.2008.10.008.

110. J. Gong, "Determining Indentation Toughness by Incorporating True Hardness Into Fracture Mechanics Equations," *Journal of the European Ceramic Society* 19, no. 8 (1999): 1585–1592, https://doi.org/10.1016/S0955-2219(98)00256-8.

111. M. Sebastiani, K. E. Johanns, E. G. Herbert, and G. M. Pharr, "Measurement of Fracture Toughness by Nanoindentation Methods: Recent Advances and Future Challenges," *Current Opinion in Solid State and Materials Science* 19, no. 6 (2015): 324–333, https://doi.org/10.1016/j.cossms.2015.04.003.

112. X. Xu, T. Cui, G. Mcconohy, et al., "Heterogeneous Doping via Nanoscale Coating Impacts the Mechanics of Li Intrusion in Brittle Solid Electrolytes," *Nature Materials* 25 (2026): 627–634, https://doi.org/10.1038/s41563-025-02465-7.

113. B. R. Lawn and E. R. Fuller, "Equilibrium Penny-Like Cracks in Indentation Fracture," *Journal of Materials Science* 10, no. 12 (1975): 2016–2024, https://doi.org/10.1007/BF00557479.

114. K. Niihara, "A Fracture Mechanics Analysis of Indentation-induced Palmqvist Crack in Ceramics," *Journal of Materials Science Letters* 2, no. 5 (1983): 221–223, https://doi.org/10.1007/BF00725625.

115. G. D. Quinn and R. C. Bradt, "On the Vickers Indentation Fracture Toughness Test," *Journal of the American Ceramic Society* 90, no. 3 (2007): 673–680, https://doi.org/10.1111/j.1551-2916.2006.01482.x.

116. Y. Feng, T. Zhang, and R. Yang, "A Work Approach to Determine Vickers Indentation Fracture Toughness," *Journal of the American Ceramic Society* 94, no. 2 (2011): 332–335, https://doi.org/10.1111/j.1551-2916.2010.04289.x.

117. A. Nastic, A. Merati, M. Bielawski, M. Bolduc, O. Fakolujo, and M. Nganbe, "Instrumented and Vickers Indentation for the Characterization of Stiffness, Hardness and Toughness of Zirconia Toughened Al_2O_3 and SiC Armor," *Journal of Materials Science & Technology* 31, no. 8 (2015): 773–783, https://doi.org/10.1016/j.jmst.2015.06.005.

118. A. Moradkhani, H. Baharvandi, M. Tajdari, H. Latifi, and J. Martikainen, "Determination of Fracture Toughness Using the Area of Micro-crack Tracks Left in Brittle Materials by Vickers Indentation Test," *Journal of Advanced Ceramics* 2, no. 1 (2013): 87–102, https://doi.org/10.1007/s40145-013-0047-z.

119. H. Peng, Y. Liu, Z. Chen, et al., "Synchrotron X-ray Topographic Characterization of Dislocations in 6H-SiC Axial Samples," *Journal of Crystal Growth* 579 (2022): 126459, https://doi.org/10.1016/j.jcrysgro.2021.126459.

120. A. Lankinen, T. O. Tuomi, O. Anttila, et al., "Synchrotron X-ray Topography Investigation on Dislocation Propagation in Heavily Arsenic-doped Silicon Crystal Necks," *Journal of Crystal Growth* 677 (2025): 128459, https://doi.org/10.1016/j.jcrysgro.2025.128459.

121. D. A. Greeley, H. T. Vo, R. J. McCabe, M. M. Schneider, C. N. Tomé, and L. Capolungo, "A Quantitative Comparison of the Fingerprint of Twinned Microstructures Through Surface and Three-dimensional Techniques," *Nature Communications* 16, no. 1 (2025): 9773, https://doi.org/10.1038/s41467-025-64740-0.